

Journal of Materials Chemistry B

Materials for biology and medicine

Accepted Manuscript

This article can be cited before page numbers have been issued, to do this please use: L. Li, A. R. Muguruza, F. M. Arrabal, T. Fernandez, N. Muñoz-Flores, S. Fernández-García, J. Lorenzo, I. Fernández, R. Contreras-Caceres and P. Guardia, *J. Mater. Chem. B*, 2026, DOI: 10.1039/D6TB00497K.



This is an Accepted Manuscript, which has been through the Royal Society of Chemistry peer review process and has been accepted for publication.

Accepted Manuscripts are published online shortly after acceptance, before technical editing, formatting and proof reading. Using this free service, authors can make their results available to the community, in citable form, before we publish the edited article. We will replace this Accepted Manuscript with the edited and formatted Advance Article as soon as it is available.

You can find more information about Accepted Manuscripts in the [Information for Authors](#).

Please note that technical editing may introduce minor changes to the text and/or graphics, which may alter content. The journal's standard [Terms & Conditions](#) and the [Ethical guidelines](#) still apply. In no event shall the Royal Society of Chemistry be held responsible for any errors or omissions in this Accepted Manuscript or any consequences arising from the use of any information it contains.

ARTICLE

Electrospun PVA-Chitosan Nanofibers with Antibacterial Properties for Wound Healing: Unveiling the Potential of Low Molecular Weight Chitosan

Liqiong Li,^{a,b} Asier R. Muguruza,^a Francisco M. Arrabal-Campos,^c Tamara Fernández,^d Silvia Fernández-García,^b Nuria Muñoz-Flores,^b Julia Lorenzo,^{d,e} Ignacio Fernández,^{b,*} Rafael Contreras-Caceres,^{b,*} Pablo Guardia^{b,*}

Received 00th January 20xx,
Accepted 00th January 20xx

DOI: 10.1039/x0xx00000x

Chitosan (CS) is a high molecular weight biopolymer derived from the deacetylation of chitin, which is naturally present in the exoskeletons of crustaceans. However, its inherently low water solubility limits many biomedical applications. In contrast, low-MW CS (LMWCS) is water-soluble and exhibits promising biological properties. Herein, we report the synthesis of two LMWCS (**CS1** and **CS7**) and their incorporation into electrospun poly(vinyl alcohol) (PVA) nanofibers (NFs) at various loadings. Both LMWCS samples were successfully integrated into PVA NFs without crosslinkers, with tunable encapsulation and release confirmed by elemental analysis, UV-vis and NMR spectroscopy. Comparative evaluations revealed that **CS7**-containing fibers exhibited superior antimicrobial efficacy against *S. aureus*, *E. coli*, *P. aeruginosa*, and *C. albicans*, and significantly promoted HaCaT-ras A5 keratinocyte migration in scratch assays. Together, this work establishes molecular weight-dependent design principles for engineering multifunctional electrospun wound dressings that integrate both antimicrobial activity and pro-regenerative capability.

1. Introduction

Chronic wounds represent a significant and growing global healthcare burden, with an amputation occurring approximately every 30 seconds as a result of persistent infection and impaired healing processes.^{1,2} Wound dressings serve as the first line of clinical treatment by providing hemostatic, anti-inflammatory, and antimicrobial effects that help reestablish a regenerative microenvironment and promote tissue regeneration.^{3,4} Nevertheless, conventional dressings often are not able to manage microbial contamination, reducing considerably the functionality to support complex cellular responses needed for effective healing. Indeed, recurrent infections perpetuate the detrimental cycle of "infection-inflammation-delayed healing", leading to prolonged hospitalization and poor therapeutic outcomes.^{5,6} These limitations highlight the urgent need for multifunctional wound dressings that can simultaneously prevent infection and accelerate tissue repair.

Among different materials for wound-dressing applications, electrospun nanofibers (NFs) have emerged as promising platforms for wound dressings due to their ability to closely mimic the structural and functional properties of the native extracellular matrix (ECM). Their high surface area-to-volume ratio, tunable porosity, and interconnected fibrous architecture facilitate gas exchange, nutrient diffusion, and cellular attachment, all of which contribute to enhanced wound healing performance.⁷⁻⁹ In this context, electrospinning is a robust and scalable technique for the fabrication of nanofibrous mats. For instance, synthetic polymers such as polycaprolactone (PCL), poly(lactic-co-glycolic acid) (PLGA), and poly(vinyl alcohol) (PVA) are frequently employed owing to their favorable mechanical properties and processability.¹⁰⁻¹² However, the limited bioactivity and biodegradability of purely synthetic polymers have motivated increasing interest in incorporating natural biopolymers to enhance biological performance.

Among natural polymers, chitosan (CS), a polysaccharide derived from the partial deacetylation of chitin, has gained significant attention in wound care due to its broad-spectrum antimicrobial activity, hemostatic properties, biodegradability, and biocompatibility.¹³⁻¹⁸ Its antimicrobial effect is generally attributed to electrostatic interactions between protonated amino groups on the polymer backbone and negatively charged microbial membranes, ultimately leading to membrane disruption and cell death.¹⁹ The antimicrobial activity is mainly modulated by the molecular weight (MW), dispersity (\mathcal{D}), and the degree of deacetylation (DD) of the CS, which also determine its solubility, viscosity, and charge density.^{20,21} In fact, the biomedical application of high-MW CS (>100 kDa) is hindered by a poor solubility, high

^a Institut de Ciència de Materials de Barcelona (ICMAB-CSIC) Campus de la UAB, 08193 Bellaterra, Spain E-mail: pguardia@icmab.es

^b Department of Chemistry and Physics, Research Centre CIAIMBITAL, University of Almería, 04120, Almería, Spain E-mail: ccc689@ual.es; ifernan@ual.es

^c Department of Engineering, Research Centre CIAIMBITAL, University of Almería, 04120, Almería, Spain

^d Institut de Biotecnologia i Biomedicina, Departament de Bioquímica i Biologia Molecular (IBB), Universitat Autònoma de Barcelona, 08193 Cerdanyola del Vallès, Barcelona, Spain

^e Centro de Investigación Biomédica en Red: Bioingeniería, Biomateriales y Nanomedicina, Spain

† Footnotes relating to the title and/or authors should appear here.



viscosity, and batch-dependent variability in acetylation patterns, which affect processability and reproducibility.²²

To overcome these limitations, significant efforts have been made to reduce the MW of CS using several methodologies, such as acid hydrolysis, enzymatic degradation, oxidative cleavage, and microwave-assisted hydrolysis.^{23–25} Among these methods, microwave-assisted hydrolysis is a rapid, environmentally friendly route to prepare low-molecular-weight CS (LMWCS, < 10 kDa) with improved water-solubility and enhanced cationic charge, offering possibilities for biomedical applications.^{26,27} Indeed, it has been demonstrated that LMWCS exhibits significantly improved antibacterial performance, with studies reporting a 4 to 8-fold increase in efficacy compared to high-MW CS when tested against *S. aureus* and *E. coli*.^{28,29} Despite these encouraging findings, most studies have either focused on chitooligosaccharides (< 3.9 kDa) or on chemically modified derivatives, whereas systematic evaluation of water-soluble LMWCS in the intermediate molecular weight range (5–10 kDa) remains scarce, leaving its MW-dependent biological effects insufficiently understood. Notably, incorporating such LMWCS into electrospun polymeric scaffolds could establish a macroscopic platform with controlled release and enhanced healing efficacy, thereby overcoming the structural instability limitations associated with conventional topical formulations such as gels or lotions.^{30,31}

Natural polymers such as CS are excellent candidates providing improved functionalities to synthetic polymers such as PVA. Typically, CS has been blended with synthetic polymers including PVA,³² poly(ethylene oxide) (PEO)³³ and polyacrylamide (PAAm)³⁴ to fabricate nanocomposite fibers or hydrogels with enhanced antimicrobial activity. Among them, PVA@CS NFs is studied due to their excellent electrospinnability, along with the potential to form hydrogen bonds between hydroxyl and amino groups, which enhances structural integrity and biological interactions.³⁵ However, most reports rely on high-MW CS (MW > 100 kDa), whose poor miscibility and limited water solubility hinder uniform fiber formation and compromise reproducibility.^{36,37} To overcome these drawbacks, recent research has focused on using LMWCS (in particular chitooligosaccharides MW < 3.9 kDa) or chemically modified CS derivatives (e.g., carboxymethyl-CS,³⁸ quaternized-CS³⁹) to improve water solubility, antimicrobial activity, and processability⁴⁰. Nevertheless, these approaches often involve multistep synthesis, toxic reagents, or raise concerns regarding biodegradability and biosafety.^{41–43} Moreover, their low MW is associated with poor mechanical strength and rapid degradation, narrowing their potential application in medicine. In this context, water-soluble LMWCS offers a key opportunity to optimize the production of CS-loaded polymer NFs, particularly regarding their loading efficiency, release kinetics, and biological performance. Accordingly, systematic studies evaluating water-soluble LMWCS within the intermediate MW window (5–10 kDa) in electrospun PVA scaffolds remain lacking.

In this study, a chitooligosaccharide CS1 of weight-averaged molecular weight (Mw) of 1.67 ± 0.28 kDa, and an LMWCS CS7 of Mw of 7.47 ± 0.62 kDa, were prepared via a microwave-assisted oxidative hydrolysis of a commercial CS of 300 kDa (CS300). For the sake of

simplicity, CS1 and CS7 will hereafter be referred to as LMWCS. The MW distribution and disaccharide unit composition of the resulting LMWCSs were characterized using ¹H molecular weight-ordered spectroscopy (MwOSY) in combination with complementary NMR analyses, enabling a detailed and internally consistent description of chitosan samples in the low-to-intermediate molecular weight range. Subsequently, the CS samples were incorporated into PVA NFs at different concentrations (5.9–23.8 wt.%) via blend electrospinning. Their release behavior from the NFs were quantitatively evaluated for the first time using a comparative approach based on both NMR and UV-vis spectroscopy. Furthermore, we investigated how MW modulates the antimicrobial activity of CS against representative bacterial and fungal species, as well as its wound-healing performance in keratinocyte migration assays. This study therefore addresses the existing gap in understanding the structure-function relationship of water-soluble LMWCS in electrospun PVA scaffolds and highlights their potential as multifunctional wound dressings.

2. Results and discussion

2.1 Synthesis and characterization of CS7 and CS1

As detailed in the Materials and methods, LMWCS were obtained from commercial CS (**CS300**) via oxidative hydrolysis using hydrogen peroxide (H₂O₂) as oxidant under microwave irradiation (**Fig. 1A**). Microwave-assisted hydrolysis enhances dipolar polarization and ionic conduction in polar media, accelerating the generation of reactive oxygen species that cleave β(1→4) glycosidic linkages in the CS backbone.^{44,45} According to the mechanism proposed by Chang et al.,⁴⁶ perhydroxyl radical anions (HOO•) react with H₂O₂ to form hydroxyl radicals (•OH) and superoxide radical anions (O₂•), which react with the glycosidic bonds, leading to MW reduction and, consequently, enhanced water solubility. In this work, by modulating microwave exposure time and temperature at a fixed H₂O₂ concentration (5% w/v), two CS samples with different MWs, here denoted as **CS1** and **CS7**, were obtained (see **Fig. 1A** and Materials and methods for details). This microwave assisted method provides a rapid and green alternative compared to conventional hydrolysis, yielding structurally intact yet highly water-soluble LMWCS suitable for biomedical applications. After synthesis, the chemical structures of **CS1** and **CS7** were initially assessed by ¹H and ¹³C NMR spectroscopy.

¹H and ¹³C NMR spectra of **CS1** and **CS7** (**Fig. 1B** and **Fig. S1**) confirmed the preservation of the polymer's chemical backbone after oxidative hydrolysis, with all samples exhibiting comparable resonance patterns.⁴⁷ In these ¹H NMR spectra, the signal located at δ_H 1.9 ppm is assigned to the methyl protons of the *N*-acetyl group of the acetylated glucosamine unit (A). The resonance at δ_H 2.6 ppm corresponds to the H2 proton of the deacetylated glucosamine unit (D). The group of peaks between δ_H 3.2 and 3.8 ppm comprises the H3–H6 protons of both A and D units, together with the H2 proton of the acetylated unit (A). Finally, the signal at δ_H 4.4 ppm is attributed to the anomeric H1 protons of both A and D units. Subsequently, pulsed-field gradient stimulated echo diffusion NMR experiments with bipolar gradient pulses (PFG-STE-BPP) were combined with inverse Laplace transform (ILT) algorithms such as dART⁴⁸ and TRAln,⁴⁹ to estimate the weight-average MW and dispersity of the



produced LMWCS. Diffusion coefficient profiles were converted into Mw distributions using universal calibration relationships that are independent of both solution viscosity⁵⁰ and polymer concentration,⁵¹ whereas the Mw and dispersity of the commercial high-MW chitosan (**CS300**) could not be determined by this approach due to its limited solubility in aqueous media.

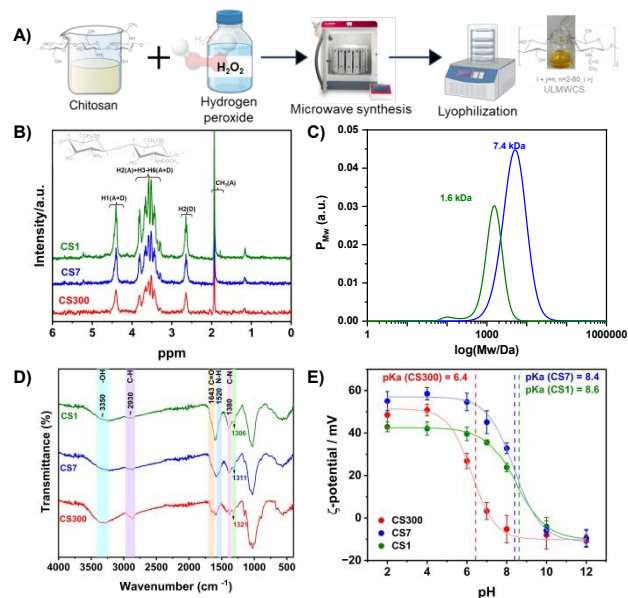


Fig. 1. A) Schematic representation of the microwave-assisted hydrolysis process to produce **CS1** and **CS7** from **CS300**. B) ^1H NMR spectra of **CS7** (blue line) and **CS1** (green line) (A: acetylated, DD: deacetylated). C) MW distribution of **CS7** (blue line) and **CS1** (green line) obtained from PGSE-STE-BPP inverse Laplace transformation (ILT) techniques (see SI). D) FTIR spectra of **CS300** (red line), **CS7** (blue line) and **CS1** (green line). E) ζ -potential measurements at different pH values in aqueous solutions for **CS300** (red line), **CS7** (blue line) and **CS1** (green line) at a constant conductivity of $0.520 \mu\text{S}/\text{cm}$.

We obtained MW distributions centered at $1.67 \pm 0.28 \text{ kDa}$ and $7.47 \pm 0.62 \text{ kDa}$ with narrow dispersities (\mathcal{D}) of 2.0 and 2.2 for **CS1** and **CS7**, respectively (**Fig. 1C** and **Table 1**). The degree of deacetylation (DD) calculated using Equations (1) and (2) included in the Materials and methods, remained relatively stable across all samples. A DD of 74.1 % for **CS300** was considered, in line with the manufacturer's specifications, while the determined for **CS7** and **CS1** showed slightly elevated values of 75.8 % and 76.6 %, respectively. This is consistent with minor acetyl group loss during hydrolysis. Overall, these data confirm that microwave-assisted oxidative cleavage effectively lowers the MW of CS without compromising its structural integrity.

Fig. 2 displays the ^1H molecular weight-ordered spectroscopy (MwOSY) maps of the LMWCS **CS1** and **CS7**. The horizontal axis (F2) reports the ^1H chemical shift (ppm), whereas the vertical axis (F1) shows the weight-average MW, MW (Da, log scale), derived from diffusion encoding and converted into MW using universal calibration relationships. The top projection corresponds to the associated ^1D ^1H spectrum, and the right-hand projection depicts the MW distribution. In both samples, the F1 projections reveal a dominant monomodal population, confirming the narrow molecular-weight distributions obtained from the diffusion-based analyses

described above, centered at approximately 1.67 kDa for **CS1** and 7.47 kDa for **CS7**. Importantly, the MW-chemical shift correlations indicate that the main chitosan resonances (N-acetyl CH3 at δH 1.9 ppm, H2 of the deacetylated unit at δH 2.6 ppm, the H3-H6/H2 region at δH 3.2-3.8 ppm, and the anomeric H1 signal at δH 4.4 ppm) all map onto the same MW range, supporting sample homogeneity and preservation of the polymer backbone after oxidative hydrolysis.

Table 1. Summary of the different parameters obtained from the NMR analysis for **CS1** and **CS7** (D: diffusion coefficient, r_H : hydrodynamic radius, \mathcal{D} : dispersity, DD: Deacetylation degree).

| | D x 10 ⁻⁹ [m ² s ⁻¹] | r _H [nm] | MW [kDa] | \mathcal{D} | DD [%] |
|------------|--|---------------------|-------------|---------------|--------|
| CS1 | 0.17 ± 0.01 | 12.5 ± 0.2 | 1.67 ± 0.28 | 2.0 ± 0.2 | 76.6 |
| CS7 | 0.11 ± 0.01 | 18.2 ± 1.0 | 7.47 ± 0.62 | 2.2 ± 0.3 | 75.8 |

The red dashed box marks the solvent suppression region (water signal, ~ 4.7 -5.0 ppm). The approach has been previously introduced and validated by some of us in other polymeric systems⁵², and to the best of our knowledge, this is the first time that ^1H MwOSY has been applied to chitosan-based polymers. For detailed experimental procedures and calculations, please refer to the Supplementary Information (SI).

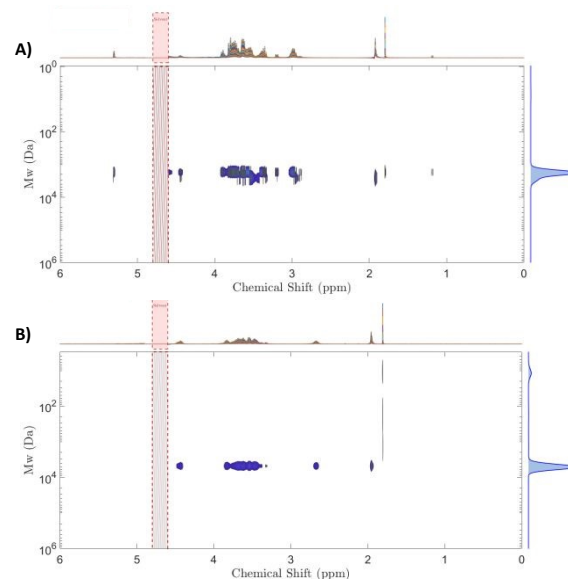


Fig. 2. ^1H molecular weight-ordered spectroscopy (MwOSY) maps of the LMWCSs **CS1** A) and **CS7** B). Red dashed boxes mark the solvent suppression region (water signal, ~ 4.7 -5.0 ppm).

The FTIR analysis for **CS300**, **CS7** and **CS1** (**Fig. 1D**) confirmed the retention of the characteristic functional groups and hydrogen-bonding network after degradation, as evidenced by the asymmetric and symmetric C-H stretching bands at 2930 and 2860 cm^{-1} , the broad -NH/-OH stretching band around 3350 cm^{-1} , and the N-acetyl-related peaks at 1643 cm^{-1} (C=O) and 1380 cm^{-1} (C-N). Notably, no absorption was observed near 1735 cm^{-1} or within 2830 - 2695 cm^{-1} , indicating the absence of carboxyl or aldehyde groups and implying that the degradation process did not induce ring-opening of glucosamine units.^{53,54} Minor shifts of the amide band and changes



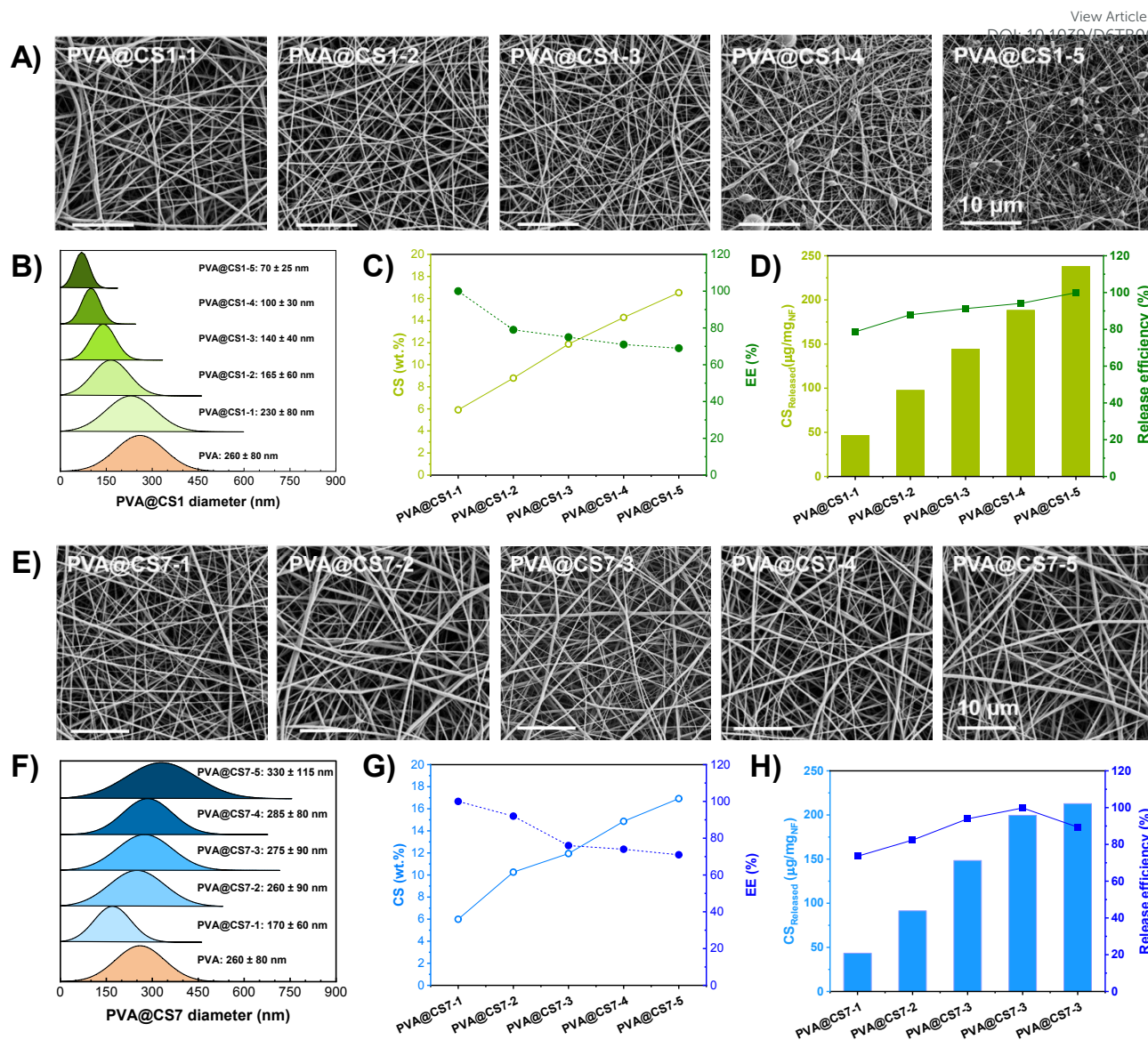


Fig. 3. Representative SEM images of PVA@CS1 A) and PVA@CS7 E) NFs obtained at different CS loadings (from 5.9 to 23.8 wt.%). Diameter size distribution of PVA@CS1 B) and PVA@CS7 F) for NFs produced at different CS loadings (from 5.9 to 23.8 wt.%). Percentage of CSs in NFs and EEs of CS1 C) and CS7 G) in PVA NFs measured from elemental analysis. Evaluation of the CS1 D) and CS7 H) release from the PVA NFs after 24h as determined by ^1H NMR analysis (see SI for quantification details and acquisition parameters).

in the intensity of N-H-related bands suggested slight variations in the DD and local hydrogen-bonding environments associated with molecular weight reduction rather than the formation of new amide groups.⁵⁵ Interestingly, in **Fig. 1D**, the signal observed at 1643 cm^{-1} , assigned to the C=O bond in the amide group, is weaker for CS1 and CS7 if it is compared with CS300. This could indicate differences in DD values. However, as was previously reported, the decrease in the C=O signal can be consequence of structural rearrangements associated with depolymerization, which include partial deamination, nitrogen loss, and changes in hydrogen-bonding interactions due to the decrease in the molecular weight.^{56–58} Indeed, here, DD values have been properly determined through ^1H -NMR analysis, which is a more appropriated technique to determine DD values. Complementary, UV-vis spectroscopy (**Fig. S2 A**) revealed similar spectral profiles for all samples, characterized by $\pi \rightarrow \pi^*$ transitions in

the 200–240 nm region and a weak band around 300 nm assigned to forbidden $n \rightarrow \pi^*$ transitions of the acetyl groups, while increased absorption intensity was observed for lower-MW samples. This may be attributed to enhanced exposure of chromophoric groups and conformational changes associated with shorter polymer chains.⁵⁹

Zeta potential (ζ -potential) measurements were employed to assess the surface charge of CS300, CS7, and CS1 across varying pH values between 2–12 (**Fig. 1E**). From those data, the $d(\zeta\text{-potential})/d(\text{pH})$ in function of pH shows pKa values of 6.4, 8.4 and 8.6 for CS300, CS7 and CS1, respectively (**Fig. S3**). Distinct differences were observed: at physiological pH (7.0–7.5), CS1 and CS7 exhibit markedly higher positive ζ -potentials (+35 mV and +45 mV, respectively) compared with CS300 (ca. +2 mV) correlating with their improved aqueous stability. This trend was further confirmed by solubility profiles (**Fig.**



S2B), where CS300 precipitates above pH 7, whereas **CS1** and **CS7** remain fully dispersed across a broad pH window (4-12). The enhanced ζ -potential and solubility of **CS1** and **CS7** can be attributed to their lower MW and reduced crystallinity, which disrupts interchain hydrogen bonding and promotes chain solvation. As previously reported, depolymerization enhances CS's solubility by dismantling crystalline domains and exposing hydrophilic functional groups.^{60,61} Although solubility and MW assessments may vary with experimental methods, CS with MW < 10 kDa consistently exhibits excellent water solubility, supporting its application in high-concentration and low-viscosity formulations in electrospinning.

Taken together, these complementary characterizations confirm that microwave-assisted oxidative hydrolysis provides a reliable route to obtain well-defined, water-soluble LMWCS. Both **CS1** and **CS7** retained the chemical backbone of the parent polymer, exhibited narrow MW distributions, and preserved high DD. FTIR and UV-vis analyses revealed no detectable degradation by-products, while ζ -potential and solubility assays demonstrated markedly improved aqueous dispersibility compared to high-MW CS. These features highlight that **CS1** and **CS7** are structurally intact, highly soluble, and positively charged biopolymers, thereby representing suitable candidates for incorporation into electrospun PVA NFs to systematically investigate MW-dependent effects on fiber morphology, release, antimicrobial activity, and wound-healing performance.

2.2 Synthesis of PVA NFs

Electrospun NFs were fabricated from PVA solutions containing different concentrations of both LMWCS **CS1** and **CS7** (see Materials and methods for details). Pure PVA solutions at 16% (w/v) produce uniform fibers with an average diameter of 260 ± 80 nm by SEM imaging (**Fig. S4**). Then, PVA@CS composite NFs were produced with incorporated **CS1** or **CS7** at different percentages (from 5.9 to 23.8 wt.%, **Table 2**) related to the starting polymeric solution. SEM images of these fabricated NFs (**Fig. 3A** and **3E**) revealed smooth, homogeneous and continuous fiber morphologies for most formulations. At higher **CS1** loadings (PVA@CS1-4, 20.0 wt.%, and PVA@CS1-5, 23.8 wt.%), bead formation was detected, whereas **CS7**-containing fibers retained uniform structures across all initial **CS7** concentrations. Fiber diameter analysis revealed opposite trends depending on MW: **CS1** incorporation progressively reduced the diameter from 230 ± 80 nm (PVA@CS1-1 with 5.9 wt.%) to 70 ± 25 nm (PVA@CS1-5 with 23.8 wt.%) (**Fig. 3B** and **S5**), whereas the incorporation of **CS7** produced an opposite trend, increasing from 170 ± 60 nm (PVA@CS7-1) to 330 ± 115 nm (PVA@CS7-5) (**Fig. 3F** and **S5**). The observed differences in NF diameter between **CS1** and **CS7** systems are closely related to variations in solution properties, particularly electrical conductivity and viscosity. On the one hand, the **CS1** solutions exhibit higher electrical conductivity (**Fig. S6A** and **B**), which enhances electrostatic repulsion and promotes jet elongation, leading to thinner fibers. However, at elevated concentrations (≥ 20 wt.%), excessive charge density may destabilize the jet, triggering Rayleigh instability and bead formation due to surface tension dominance.⁶²⁻⁶⁴

On the other hand, the viscosity of the solutions was measured prior to electrospinning. **Fig. S6C** and **D**, shows the dynamic viscosity of

polymeric solutions containing increasing CS contents (from 5.9 to 23.8%) for **CS1** and **CS7**. Opposite trends were observed depending on the CS molecular weight. For **CS1**-based solutions, the dynamic viscosity decreases with increasing **CS1** content. This reduction in viscosity facilitates greater jet stretching, resulting in thinner nanofibers,⁶⁵ as confirmed by the SEM images in **Fig. 3A** and the diameter analysis in **Fig. 3B**. At the highest **CS1** content (23.8%), bead formation is also observed. In contrast, increasing the **CS7** content leads to higher kinematic viscosity, likely due to enhanced chain entanglement.⁶⁶ These more viscous solutions improve jet stability and limit elongation, producing nanofibers with larger average diameters, as confirmed by the SEM images in **Fig. 3E**. This trend is in well agreement with the reported literature.⁶⁷⁻⁶⁹

These findings demonstrate that fiber morphology and thickness can be effectively modulated by adjusting the MW and concentration of CS, providing a tunable platform for designing nanofibrous scaffolds with tailored dimensions and surface characteristics.

Table 2. Summary of the feeding amounts of **CS1**, **CS7**, and PVA used in the production of PVA@CS NFs. Theoretical weight percentages of CS and PVA in the NFs. Nitrogen weight percentages calculated from theoretical and elemental analyses. Mass of CS in PVA@CS NFs calculated from the nitrogen content.

| | Mass PVA [mg] | Mass CS [mg] | CS in NFs (Theor.) [wt.%] | PVA in NFs [wt.%] | N _{Theor.} [wt.%] | N _{Exp.} [wt.%] | CS in NFs (Exp.) [wt.%] |
|-----------|---------------|--------------|---------------------------|-------------------|----------------------------|--------------------------|-------------------------|
| PVA@CS1-1 | 1600 | 100 | 5.9 | 94.1 | 0.48 | 0.49 | 5.9 |
| PVA@CS7-1 | | | | | | 0.49 | 6.0 |
| PVA@CS1-2 | 1600 | 200 | 11.1 | 88.9 | 0.91 | 0.72 | 8.8 |
| PVA@CS7-2 | | | | | | 0.84 | 10.3 |
| PVA@CS1-3 | 1600 | 300 | 15.8 | 84.2 | 1.29 | 0.97 | 11.9 |
| PVA@CS7-3 | | | | | | 0.98 | 11.9 |
| PVA@CS1-4 | 1600 | 400 | 20 | 80 | 1.64 | 1.17 | 14.3 |
| PVA@CS7-4 | | | | | | 1.21 | 14.9 |
| PVA@CS1-5 | 1600 | 500 | 23.8 | 76.2 | 1.95 | 1.35 | 16.5 |
| PVA@CS7-5 | | | | | | 1.38 | 16.9 |

2.3 Spectroscopic analysis of NFs

FTIR and UV-vis spectroscopies were employed to investigate the composition, chemical structure and intermolecular interactions within the fabricated PVA@CS1 and PVA@CS7 NFs. The FTIR spectra (**Fig. S7A** for **CS1** and **S7C** for **CS7**) retained broad O-H and N-H stretching bands ($3300-3400$ cm⁻¹) characteristic of both CS and PVA. The amide I (~ 1650 cm⁻¹) and amide III (~ 1380 cm⁻¹) peaks of CS showed reduced intensities in the composite NFs, which may reflect the lower CS content relative to pure CS samples. Simultaneously, bands associated with PVA including C-O-C stretching ($\sim 1080-1150$ cm⁻¹) and CH₂ symmetric and asymmetric stretching (~ 2900 cm⁻¹) also weakened with increasing CS incorporation, likely due to the corresponding reduction in PVA concentration. No significant spectral shifts were observed between pure CS and PVA@CS NFs, indicating that blending occurred primarily through non-covalent interactions, without significant alterations to the chemical backbones. The UV-vis spectra of PVA@CS NFs (**Fig. S7B** for **CS1** and **Fig. S7D** for **CS7**) showed strong absorbance bands characteristic of CS in the 200 to 220 nm range, corresponding to $\pi \rightarrow \pi^*$ transitions together with broad and weak bands located at ca. 300 nm



corresponding to the already mentioned forbidden $n \rightarrow \pi^*$ transitions. Absorbance intensity increased with CS content in both cases. These findings collectively suggest that **CS1** and **CS7** maintained their structural features after electrospinning.

2.4 CS Loading and release

The amount of CS incorporated into PVA@CS1 and PVA@CS7 NFs was quantified by elemental analysis based on the nitrogen content, which is only present in CS (Table 2 and Table 3). The theoretical nitrogen percentages of **CS1** and **CS7** were calculated to be 8.2 % for both CSs based on their DD (see Section S1.2). Experimental nitrogen values from NFs were compared with theoretical estimates, and their ratio was defined as the encapsulation efficiency (EE). Details of the calculations, including the mass of PVA and CS used in electrospinning, theoretical and experimental nitrogen content, and the equations employed, are provided in Section S1.1 and Table 2 of the SI. As shown in Table 3, Figs. 3C and 3G, the experimental CS content in PVA@CS1 NFs increased linearly with the initial feed, ranging from 5.91% in PVA@CS1-1 to 16.53% for PVA@CS1-5. A similar trend was observed for **CS7** NFs with an increase of 5.99% (PVA@CS7-1) to 16.92% (PVA@CS7-5). However, the EE decreased with increasing CS concentration in both cases: from 100 % for PVA@CS1-1 to 69 % for PVA@CS1-5, and from 100% for PVA@CS7-1 to 71% for PVA@CS7-5. This reduction indicates that increasing the amount of CS in the reaction solution compromises the final EE. Likely, the limited miscibility of CS and the increase in viscosity with higher CS concentrations lead to phase separation during electrospinning, which ultimately affects CS distribution along the injection front (Fig. S8). This results in a non-homogeneous CS distribution along the radius, as well as CS losses during the electrospinning process.

As anticipated, increasing the amount of CS in the electrospinning solution resulted in higher CS incorporation into the final NFs, as observed for both PVA@CS1 and PVA@CS7 NFs. However, the EE decreased monotonically with increasing CS content (Table 3, Figs. 3C and 3G), indicating reduced retention efficiency at higher loadings. This behavior can be attributed to the combined effects of solution polarity and viscosity on electrospinning dynamics.^{70,71} These trends are consistent with the morphologies observed by SEM (Figs. 3A and 3E) and emphasize that MW, CS concentration, and electrostatic spinning behavior determine the encapsulation properties. Precise optimization of these parameters allows for an optimized tailoring of NFs.

As mentioned, the release of CS from PVA@CS NFs was evaluated in water at room temperature over 24 hours through NMR spectroscopy measurements (see Materials and methods, Section S1.4 and S1.5 for details). Figs. 3D and 3H show the released mass of **CS1** and **CS7** profiles for **CS1**- and **CS7**-loaded NFs, and the corresponding release data are summarized in Table 3 and Table S1. As expected, the released mass and release efficiency increased with the initial CS content. For **CS1**-containing NFs, the released CS ranged from 46.4 μg **CS1**/mg NFs for PVA@CS1-1 to 237.8 μg **CS1**/mg NFs for PVA@CS1-5 (Fig. 3D and Table S1). A similar trend was observed for **CS7**-containing NFs, with released amounts increasing from 43.4 μg **CS7**/mg NFs for PVA@CS7-1 to 212.8 μg **CS7**/mg NFs for PVA@CS7-5. Regarding the polymeric matrix, the extent of PVA dissolution, as

quantified by ^1H NMR (Table S1 and Fig. S9), decreased as the CS content in the electrospinning solution increased. This behavior is consistent with the lower relative amount of PVA present in the final NFs at higher CS loadings and indicates a stabilizing effect of CS incorporation on the nanofibrous matrix, in agreement with previous reports.^{72,73}

Table 3. Summary of theoretical and experimental CS content in the NFs (wt.%), EE, CS released and CS release efficiency evaluated after 24 h incubation by ^1H NMR.

| | CS in NFs (Theo.) [wt.%] | CS in NFs (Exp.) [wt.%] * | EE [%] | CS Released [wt.%] | CS Release Efficiency [%] |
|-----------|--------------------------|---------------------------|--------|--------------------|---------------------------|
| PVA@CS1-1 | 5.88 | 5.91 | 100 | 4.64 | 78.64 |
| PVA@CS1-2 | 11.11 | 8.79 | 79 | 9.76 | 87.93 |
| PVA@CS1-3 | 15.79 | 11.87 | 75 | 14.42 | 91.27 |
| PVA@CS1-4 | 20.00 | 14.28 | 71 | 18.82 | 94.1 |
| PVA@CS1-5 | 23.81 | 16.53 | 69 | 23.78 | 99.92 |
| PVA@CS7-1 | 5.88 | 5.99 | 100 | 4.34 | 73.56 |
| PVA@CS7-2 | 11.11 | 10.26 | 92 | 9.14 | 82.34 |
| PVA@CS7-3 | 15.79 | 11.94 | 76 | 14.84 | 93.92 |
| PVA@CS7-4 | 20.00 | 14.86 | 74 | 19.96 | 99.8 |
| PVA@CS7-5 | 23.81 | 16.92 | 71 | 21.28 | 89.41 |

*Calculated from the nitrogen content obtained from elemental analysis (see Table 2).

With the aim of comparing differences in the release behavior of PVA@CS NFs, the release kinetics of **CS1** and **CS7** were investigated by UV-vis spectroscopy. Two CS loadings within the PVA NFs were selected for these experiments, namely 11.1 wt.% (PVA@CS1-2 and PVA@CS7-2) and 23.8 wt.% (PVA@CS1-5 and PVA@CS7-5), as these compositions showed the most pronounced differences in the antibacterial and wound-healing assays discussed in the following sections. Fig. S10 shows the UV-vis spectra of CS released from the PVA@CS NFs as a function of time. The release of CS was monitored by following the absorbance at 210 nm, corresponding to the characteristic absorption peak of chitosan, for both **CS1** and **CS7**, and the corresponding kinetic profiles are shown in Fig. 4.

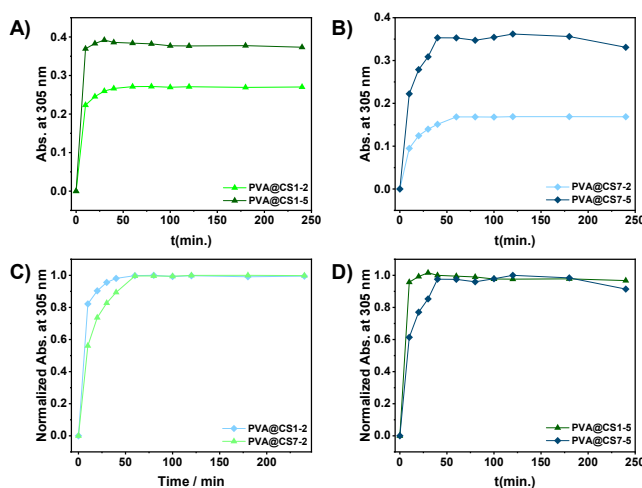


Fig. 4. Absorbance intensity at 210 nm for CS released in PVA@CS NFs fabricated with different CS percentages. A) PVA@CS1-2 and PVA@CS1-5, B) PVA@CS7-2 and PVA@CS7-5. C) and D) show normalized absorbance intensity at 210 nm for CS released in PVA@CS NFs at the same percentages.



First, the release behavior of NFs containing different CS loadings was compared. **Figs. 4A and 4B** display the absorbance profiles of **CS1** and **CS7** released from PVA@CS NFs containing 11.1 wt.% (light-coloured lines) and 23.8 wt.% (dark-coloured lines) CS, respectively. As expected, in both cases a higher absorbance intensity was observed for NFs with higher CS content, in agreement with the quantitative NMR analysis discussed above. Differences in the release kinetics as a function of CS MW were further analyzed by comparing **CS1** and **CS7** at identical loadings. **Figs. 4C and 4D** show the normalized release profiles for **CS1** and **CS7** at 11.1 wt.% and 23.8 wt.% CS, respectively. Notably, at low loading, **CS1** exhibited a faster release than **CS7**, indicating that LMWCS diffuses more rapidly from the PVA nanofibrous matrix. This behavior can be attributed to the shorter chain length and higher mobility of **CS1**, which facilitate its diffusion through the hydrated polymer network. However, at higher CS loadings, the release behaviour of PVA@CS NFs is also influenced by their microstructural organization. In particular, LMWCS **CS1** tends to form a denser CS-rich phase with stronger intermolecular interactions with PVA, which partially hinders mass transport and modulates the release kinetics, whereas the higher-MW **CS7** does not exhibit such pronounced structural effects.

2.5 Antimicrobial Activity

2.5.1 Antimicrobial Activity of CS and PVA

The antimicrobial activity of **CS300**, **CS7**, **CS1** and PVA was evaluated against a range of representative bacterial species (*S. aureus*, *E. coli* and *P. aeruginosa*) and a representative fungal species (*C. albicans*).⁷⁴ Minimal inhibitory concentrations (MICs) were determined using the standard broth-dilution method (**Table 4**, **Figs. S11 and S12**).⁷⁵ As expected, PVA exhibited no antimicrobial activity at concentrations up to 60 mg/mL, consistent with its chemical inertness and non-cationic nature. **CS300** exhibited limited antimicrobial activity, showing measurable effects only against *S. aureus* (MIC = 30 mg/mL) and *C. albicans* (MIC = 15 mg/mL). In contrast, a reduction in MW led to a marked enhancement of CS antimicrobial efficacy. In particular, **CS7** displayed a fourfold decrease in MIC against *S. aureus* (7.5 mg/mL) and *C. albicans* (2.5 mg/mL), and an eightfold reduction against *E. coli* (3.2 mg/mL) compared with **CS300**. **CS1**, although slightly less active than **CS7**, consistently exhibited lower MIC values than **CS300** across all tested microorganisms.

The superior activity observed for **CS7** can be correlated with its higher positive ζ -potential at physiological pH (**Fig. 1E**), which favors stronger electrostatic interactions with negatively charged microbial membranes and facilitates membrane destabilization.⁷⁶ By contrast, the generally lower activity against *P. aeruginosa* to CS-based materials is consistent with its well-documented intrinsic resistance mechanisms, including the secretion of extracellular lipopolysaccharides that sequester cationic agents and structural modifications of the lipid A region of lipopolysaccharides that stabilize divalent cations and reinforce membrane integrity.^{77–79} Although **CS1** shares similar ζ -potential with **CS7**, its short chain length may limit its ability to induce extensive membrane disruption, supporting previous hypotheses that very LMWCS may interact differently with microbial membranes.⁸⁰ Furthermore, antifungal activity was reduced when assays were conducted in LB medium (pH 7.4) compared with acidic Sabouraud medium (pH 5.5), in agreement

with the lower degree of protonation of amino groups at neutral pH and the consequent decrease in cationic charge density, which weakens electrostatic interactions with the fungal cell wall (**Table S2**). As already mentioned, these findings point out the combined influence of MW, charge density, and microorganism-specific membrane architecture in governing the antimicrobial performance of CS-based biopolymers.

Table 4. Minimum inhibitory concentration (MIC, mg/mL) of PVA, **CS300**, **CS7**, and **CS1** against *S. aureus*, *E. coli*, *P. aeruginosa*, and *C. albicans*. MICs were determined by the two-fold dilution method at 37 °C in LB (bacteria) or Sabouraud (fungi) media. Values represent three biological replicates.

| | <i>S. aureus</i> | <i>E. coli</i> | <i>P. aeruginosa</i> | <i>C. albicans</i> |
|-------|------------------|----------------|----------------------|--------------------|
| PVA | > 60 | > 60 | > 60 | > 60 |
| CS300 | 30 | 60 | > 60 | 15 |
| CS7 | 7.5 | 3.2 | 7.5 | 2.5 |
| CS1 | 15 | 15 | 30 | 7.5 |

2.5.2 Antibacterial performance of NFs

The antimicrobial activity of electrospun PVA@CS1 and PVA@CS7 NFs was evaluated using agar contact assays against *S. aureus*, *E. coli*, *P. aeruginosa*, and *C. albicans*. Discs (~2 cm diameter) prepared with two CS loadings (11.1 and 23.8 wt.%, **Table 2**) were placed on agar plates inoculated with 10³-10⁴ CFU of each microorganism. Following 24 h of incubation, colony-forming units (CFUs) beneath the discs were quantified. In specific, the antimicrobial performance of PVA@CS1-2, PVA@CS1-5, PVA@CS7-2 and PVA@CS7-5 was determined using PVA NFs as the control experiment (**Fig. 5A**). As expected, PVA NFs exhibited no antimicrobial effect, while CS-containing NFs demonstrated a concentration-dependent inhibition of microbial growth. Among all the samples tested, PVA@CS7-5 demonstrated the highest efficacy, reducing CFUs by 93 ± 13% (*S. aureus*), 95 ± 6% (*E. coli*), 87 ± 22% (*P. aeruginosa*), and 87 ± 13% (*C. albicans*) (**Fig. 5B**). This superior performance is consistent with the CS loading and release profiles, which demonstrated higher CS content and release efficiency in PVA@CS7-5. By comparison, PVA@CS1-5 showed lower reductions in microbial growth: 68 ± 9%, 74 ± 5%, 67 ± 23%, and 45 ± 7%, respectively. These outcomes are consistent with MIC data (**Table 4**) as well as the loading and release results (**Fig. 2**) and highlight again the influence of CS MW on antimicrobial activity within NF matrices.

Given the superior antimicrobial performance of PVA@CS7 NFs observed in preliminary evaluations, we systematically assessed the antibacterial efficacy of a series of PVA@CS7 NFs (1 to 5) against the Gram-negative model bacteria *E. coli*. As shown in **Fig. 5C**, inhibition followed a dose-dependent trend consistent with **CS7** release profiles (**Figs. 3H and S9**). Visual observations and CFU quantification (**Figs. S13 and S14**) revealed a strong inverse correlation between **CS7** release and viable bacterial count: samples releasing ~0.23 mg/disc of **CS7** reduced CFUs by ~72%, while those releasing ~0.30 mg/disc nearly eradicated bacterial growth. Interestingly, PVA@CS7-4 achieved the greatest antibacterial effect despite not having the highest **CS7** loading, attributable to its optimal release efficiency. These results highlight the critical role of MW and release kinetics in antimicrobial performance. While **CS1** offers more available amino



groups due to its shorter chains and increased mobility, **CS7**'s intermediate MW promotes better matrix retention, controlled release, and prolonged membrane interaction, enhancing overall efficacy. This mirrors previously observed MIC trends, where higher-MW CS demonstrates greater affinity for bacterial membranes through electrostatic interactions between protonated $-NH_3^+$ moieties and negatively charged cell surfaces, ultimately disrupting membrane integrity, releasing intracellular components, and causing cell death.^{81–83}

2.6 Wound-healing properties

View Article Online

DOI: 10.1039/D6TB00497K

2.6.1 Evaluation of wound-healing properties of PVA, CS1 and CS7.

To preliminarily evaluate the regenerative potential of **CS7** prior to its integration into nanofibrous scaffolds, we performed *in vitro* scratch assays on HaCaT-ras A5 keratinocytes using PVA, **CS1**, and **CS7** at concentrations of 0.01, 0.1, and 1 mg/mL. As shown in **Fig. 6**, **CS7** significantly enhanced wound closure compared to **CS1** and PVA, with a clear dose-dependent trend. At 0.1 mg/mL, **CS7** achieved near-complete closure within 48 hours (**Fig. 6C and D**), and the corresponding wound-healing rate reached approximately 26 ± 2 $\mu\text{m}/\text{h}$, markedly surpassing **CS1** ($\sim 19 \pm 4$ $\mu\text{m}/\text{h}$) and PVA ($\sim 10 \pm 1$ $\mu\text{m}/\text{h}$) under equivalent conditions (**Fig. 6A, B and D**). Notably, PVA-treated samples only induced marginal improvements over the untreated control (9 ± 2 $\mu\text{m}/\text{h}$), underscoring the limited intrinsic regenerative capacity of the polymer. More significantly, no adverse effects were observed when **CS1** and **CS7** were employed. Investigated concentrations are higher than the maximum CS released from developed NFS, inferring that PVA@CS NFS would not exhibit cytotoxic effects under the experimental conditions tested. These quantitative findings were visually supported by **Fig. S15**, which provides representative optical micrographs of the scratch closure process under different treatment conditions.

Cells treated with **CS7** exhibited enhanced migration into the wound area over time, whereas PVA and **CS1** treatments showed moderate or delayed closure dynamics. While **CS1** displayed some pro-healing capacity, its effect plateaued at lower concentrations and did not match the efficacy of **CS7**. The enhanced wound-healing properties of LMWCS has been previously reported.⁸⁴ W. Niu *et al.* studied the anti-inflammatory response of different CS with a MW ranging from 3 kDa to 200 kDa.⁸⁵ Lowest MW CS could be able to reach intracellular compartment and affect cells' growth and metabolism and reduce the levels of cytokines TNF- α and IL-6^{86,87}. Cell adhesion is also enhanced in the presence of CS molecules, due to the electrostatic interaction between the amine groups of the CS and the cell membrane. Furthermore, CS has been shown to activate other key-wound healing signaling pathways, including MAPK/ERK and PI3/Akt.^{88,89} These pathways' activation alongside the ability of CS to increase the availability of growth factors, promotes the creation of microenvironments that support keratinocyte proliferation and survival.⁹⁰ Interestingly, the wound-healing mechanism of ca. 1 kDa CS has not been described yet. As **CS**'s degree of polymerization is 9–2, its wound-healing mechanism could be closer to the **CS**'s monomer. T. Minagawa *et al.* described decreased wound-healing abilities of *N*-acetylated and deacetylated glucosamine monomers compared with LMWCS.⁹¹ Molecular analysis on the inflammatory response of dermal fibroblast cells in the presence of monomers revealed and increased levels of the inflammatory factor IL-8.⁹²

These results establish **CS7** as a potent wound-healing agent and provide a strong rationale for its incorporation into PVA-based electrospun NFS, enabling the dual delivery of antimicrobial and pro-regenerative functionalities.

2.6.2 Evaluation of wound-healing properties of NFS

The wound healing potential of PVA@CS7 NFS was assessed through *in vitro* keratinocyte migration assays using formulations containing 11.1% and 23.8% **CS7** (PVA@CS7-2 and PVA@CS7-5). As shown in **Fig.**

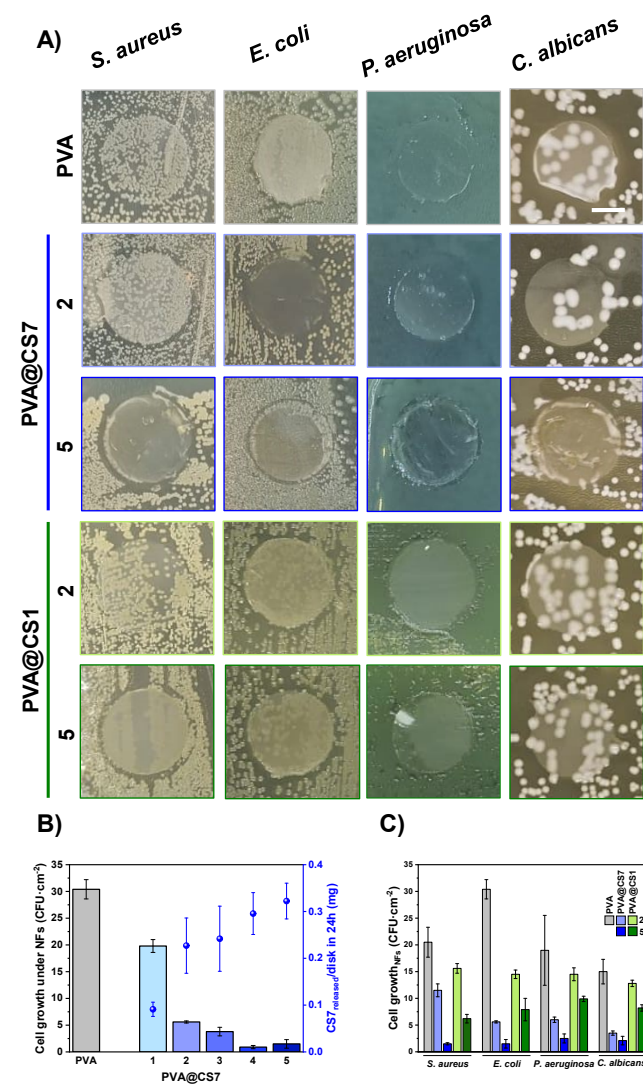


Fig. 5. Antimicrobial performance of PVA@CS1-2, PVA@CS1-5, PVA@CS7-2, and PVA@CS7-5. A) Representative photographs of LB agar plates of *S. aureus* (ATCC 12260), *E. coli* (K12) and *P. aeruginosa* (PA01) and Sabouraud agar plates of *C. albicans* (ATCC 10231) incubated with different PVA composites overnight at 37 °C. Scale bar represents 1 cm. B) Enumeration of the Colony Forming Units (CFU) under the composites. C) The relationship between quantitative values of colony forming units (CFUs) of *E. coli* in the presence of PVA@CS7 (**Fig. S14**) disks and the estimated release of **CS7** from each disk. The results described (mean \pm SD) are based on 3 biological replicates.



6F, PVA@CS7-5 significantly accelerated wound closure, with the wound nearly sealed within 48 hours. The estimated healing rates (**Fig. 6G**) increased from $9 \pm 1 \mu\text{m}/\text{h}$ (untreated) to $16 \pm 3 \mu\text{m}/\text{h}$ and $20 \pm 4 \mu\text{m}/\text{h}$ for PVA@CS7-2 and PVA@CS7-5, respectively. These results were consistent with enhanced cellular migration observed in supplementary microscopy images (**Fig. S16**) and correlate well with the dose-dependent **CS7** release profiles (**Fig. 6G**).

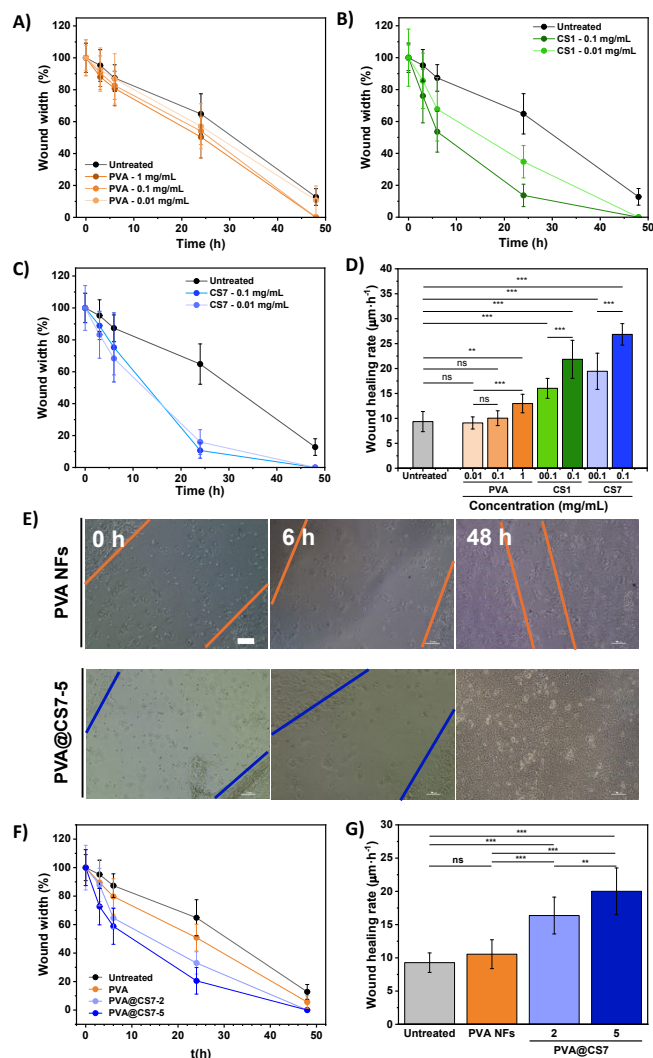


Fig. 6. Wound healing assays of control compounds and developed NFs with HaCaT-ras A5 cells. Quantification of wound closure of HaCaT-ras A5 cells incubated with different concentration of A) PVA, B) CS1 and C) CS7, and D) estimated would healing rate. E) Representative images of HaCaT-ras A5 cell proliferation in the presence of the explored PVA and PVA@CS7-5 NFs (Scale bar = 100 μm). F) Quantification of the wound width over time and G) the estimated wound healing rate. Statistical significance was determined by one-way ANOVA, ns: $p > 0.05$, *: $0.05 > p > 0.01$, **: $0.01 > p > 0.001$, and ***: $p < 0.001$

These findings suggest that **CS7** retains its pro-regenerative bioactivity after electrospinning and supports keratinocyte proliferation and migration, likely through mechanisms involving its cationic nature, antioxidant properties, and promotion of cellular adhesion.^{93,94} The fibrous structure of PVA@CS7 NFs additionally mimics the extracellular matrix, providing topographical cues that facilitate directional migration and tissue integration.^{95,96} Compared

with **CS1**, which showed moderate healing capacity in soluble form but lacked robust antimicrobial function, **CS7** offers a more advantageous multifunctional profile. These results reinforce the potential of PVA@CS7 NFs as bioactive wound dressings capable of simultaneously supporting tissue repair and infection control.

PVA@CS NFs have been previously postulated as wound healing composites,⁹⁷ nevertheless, the high-MW CS employed hindered their activity, requiring the addition of other ROS scavenging components (cerium oxide nanoparticles,⁹⁸ curcumin⁹⁹ or acrolein¹⁰⁰) to bust their wound healing activity, and limiting CS's role to structural level. For instance, wound closure of ca. 40 % were achieved, after 24 h, by H. Liu *et al.*⁹⁸ using CS with Mw = 50-190 kDa, half of the activity of PVA@CS7-5 NFs. CS NFs have been primarily employed as scaffolds for tissue regeneration rather than for wound healing due to the CS's low water solubility.^{101,102} Finally, CS has been incorporated into other types of soft composites.¹⁰³⁻¹⁰⁵ Y. Tan *et al.* reported the *in situ* formation of caffeic acid and hydroxypropyl functionalized CS (MW = 100-200 kDa) and dextran hydrogel in the wound site, with a wound closure after 24 h of ca. 45 %. Nevertheless, these approaches require further chemical modification of CS.

3. Conclusion

This work presents a comprehensive investigation into the design of electrospun PVA NFs composites incorporating LMWCS as a multifunctional agent for antibacterial and wound-healing applications. Two well-defined water-soluble CS molecules, **CS1** (1.67 ± 0.28 kDa) and **CS7** (7.47 ± 0.62 kDa), were obtained via microwave-assisted oxidative hydrolysis and structurally characterized to ensure chemical integrity, narrow Mw dispersities, and enhanced solubility. Indeed, this work applies for the first time ¹H MwOSY to the characterization of underexplored chitosans of low-molecular weight. Both CS were successfully integrated into electrospun PVA NFs without the need for chemical crosslinkers, and their encapsulation, release, and biological properties were systematically evaluated. Notably, NFs containing **CS7** (PVA@CS7) demonstrated superior antimicrobial and wound healing performances over **CS300** and **CS1**. The PVA@CS7 NFs exhibited enhanced morphological stability, with similar EE, and tunable release kinetics for PVA@CS1 NFs, features that translated into outstanding antimicrobial activity against both Gram-positive and Gram-negative bacteria, as well as fungi. This antimicrobial efficacy was correlated strongly with *in situ* **CS7** release along with the elevated surface charge and membrane-disruptive potential of this CS. Furthermore, **CS7** preserved its pro-regenerative activity after incorporation into PVA NFs, significantly accelerating keratinocyte migration and wound closure *in vitro*.

Together, these findings highlight the potential of PVA@CS7 NFs as a scalable, crosslinker-free, and bioactive wound dressing platform overcoming the standard issues of solubility and variability challenges associated with conventional CS. Moreover, this work reveals the underexplored potential of LMWCS (3.9 to 10 kDa) to simultaneously fulfill structural, antimicrobial, and regenerative roles in fiber-based biomaterials. The approach offers a sustainable and reproducible strategy to engineer multifunctional dressings, bridging



the gap between high-performance synthetic matrices and biologically responsive natural polymers.

4. Experimental section

4.1 Materials

Commercial high-MW CS (**CS300**, MW = 100-300 kDa; >75% deacetylated) was purchased from Fisher Scientific (Waltham, MA, USA). Polyvinyl alcohol (PVA, MW = 89-98 kDa, 98-99% hydrolyzed), sodium hydroxide (NaOH), *N,N'*-dimethylformamide (DMF), hydrogen peroxide (H₂O₂, 30%, w/v), sodium chloride (NaCl), Phosphate Buffered Saline (PBS) solution (0.1M, pH 7.4), ethylenediaminetetraacetic acid disodium salt dihydrate (Na₂EDTA·H₂O), Propidium Iodide (PI) and Sabouraud dextrose agar (2% dextrose) media were purchased from Merck Sigma-Aldrich (St Louis, MO, USA). Deuterium oxide (D₂O) and acetic acid-d (CD₃COOD) were purchased from Eurisotop (Saint-Aubin, France). Ethanol (EtOH, 96% v/v for clinical diagnosis) was purchased from PanReac ApplicChem (Barcelona, Spain). Acetic Acid (AcOH, glacial 99.8% AGR ACS ISO Reag. Ph. Eur.) was supplied by Labkem (Barcelona, Spain). European bacteriological agar, triptone, pentose, glucose, and yeast extract were purchased from Condalab (Madrid, Spain). All aqueous solutions were prepared with Milli-Q water (Millipore purification system, Millipore, Burlington, MA, USA). All chemicals were used as received without further purification.

4.2 Preparation of water-soluble LMWCS

LMWCS, here denoted as **CS1** and **CS7**, with different MW were initially prepared by following a previously reported microwave-assisted H₂O₂ hydrolysis method with minor modifications.¹⁰⁶ Briefly, 600 mg of high MW CS (**CS300**) was dissolved in 20 mL of 2% (v/v) acetic acid under continuous magnetic stirring overnight at room temperature. Then, a 30% (w/v) H₂O₂ solution was added to achieve a final concentration of 5% (w/v). The mixture was subjected to microwave irradiation (Milestone flexi WAVE, Milestone™ Srl, Sorisole, Italy) at 600 W under two different conditions to obtain distinct MW: 80 °C for 20 min for **CS7** and 100 °C for 30 min for **CS1**. After cooling, the solution was neutralized to pH 7-8 with 10 M NaOH and centrifuged at 6000 rpm for 15 min to remove insoluble residues. The supernatant was mixed with 100 mL of ethanol and kept at 4 °C overnight to induce precipitation. The precipitate was collected by centrifugation (6000 rpm, 10 min), freeze-dried at -80 °C for 24 h, and stored in a desiccator until use.

4.3 Electrical conductivity of polymer solutions for electrospinning

The electrical conductivity of the polymeric solutions was measured using a digital conductimeter (Conductimeter Basic 30, CRISON Instruments, Spain) at room temperature. Prior to measurement, the instrument was calibrated with standard conductivity solutions of 147 μS/cm and 12.88 mS/cm. Each solution was measured in triplicate, and the reported values represent the average conductivity, which was used to evaluate the effect of COS type and concentration on the properties of the electrospinning solutions (Fig. S6).

4.4 Preparation of PVA NFs and PVA@CS NFs:

Electrospun NFs were fabricated using a microfluidics electrospinning apparatus (Doxa Microfluidics, Málaga, Spain), as is shown in Fig. S17. For the preparation of PVA@CS composite NFs, polyvinyl alcohol (PVA, 16% w/v) was firstly dissolved in an aqueous solution containing 5% (v/v) dimethylformamide (DMF) and 1% (v/v) acetic acid (AcOH) at 80 °C under constant magnetic stirring for 6 h. Subsequently, **CS1** or **CS7** was added at concentrations ranging from 1% to 5% (w/v), and the mixture was stirred overnight at room temperature to ensure complete homogenization. After that, 5 mL of the final polymeric solution was loaded into a 10 mL plastic syringe for the electrospinning process. At this point, the polymeric solution was delivered at a flow rate of 0.68 mL/h through the injector, which is a metal needle (0.9 mm outer diameter (OD), and 0.6 mm inner diameter (ID) connected to a PTFE capillary (OD 1.6 mm, ID 0.8 mm). Then, in order to form the Taylor cone, electrospinning was performed under a constant voltage of 23 kV, with a 15 cm distance between the needle tip and the collector. The NFs were collected on a 20 cm diameter stainless-steel disk covered with aluminum foil. For uniform fiber deposition, electrospinning was conducted for 3 h until a 12 cm diameter circular area of NFs was formed. Control PVA NFs were fabricated under identical conditions using the same solvent composition but without CS. All experimental formulations, including specific quantities of PVA, CS, DMF, AcOH, and water, are summarized in Table S3. The samples were designated according to the CS employed and its concentration in the solution. For example, NFs containing 5% (w/v) **CS1** were labeled as PVA@CS1-5.

4.5 Physicochemical characterization

MW of CS1 and CS7: The MW of synthesized **CS1** and **CS7** was determined by pulsed-field gradient stimulated echo (PFG-STE) diffusion NMR. Nuclear magnetic resonance (NMR) measurements were performed using a Bruker Avance III HD 500 NMR spectrophotometer (Bruker BioSpin GmbH, Germany). CS samples (ca. 1 mg) were dissolved in 0.5 mL of D₂O and placed into a 5 mm NMR tube. The experimental setups during the NMR analyses are detailed in Section S1.2 and Section S1.3. The weight-averaged MW distributions were estimated from the measured diffusion coefficients obtained, using established calibration procedures. The inverse Laplace transform of the diffusion decay data to recover the distribution profile was performed using the TRAI and dART algorithms.

¹H NMR and ¹³C NMR analysis: NMR spectra were recorded at 298 ± 0.1 K on a Bruker Avance HD III 500 spectrometer operating at a proton frequency of 500.13 MHz using a 5 mm broad band BBFO (1H/BB-19F) pulse field gradient probe head. The spectrometer transmitter was locked to CDCl₃ frequency. Spectra were acquired and processed using TOPSPIN software (version 3.6.4). ¹H and ¹³C chemical shifts are referenced relative to tetramethylsilane (TMS). The NMR samples were prepared by adding 20 mg of CS1 or CS7 to 0.5 mL of CDCl₃.

Determination of Degree of N-acetylation (DA): The degree of N-acetylation (DA) of **CS1** and **CS7** was calculated from ¹H NMR spectra acquired using the water-presaturation pulse sequence (Bruker NOESY-presaturation, noesygppr1d, Bruker BioSpin GmbH, Germany). This sequence applies continuous-wave irradiation to selectively presaturate and suppress the water resonance during



both the relaxation delay and mixing time, effectively removing the water signal from the spectrum. Acquisition parameters were as follows: spectral width, 15.0 ppm centered at 4.70 ppm; relaxation delay (d1), 10 s; mixing time (d8), 30 ms; power-switching delay (d12), 20 μ s; gradient-recovery delay (d16), 200 μ s; acquisition time, 2.0 s; and number of scans per FID, 80. Pulse widths were p0 = 10.43 μ s (30° excitation pulse), p1 = 11.20 μ s (90° high-power pulse), and p16 = 1000 μ s (homospoil gradient pulse). Presaturation was delivered at the low-power level p19 (3.66 $\times 10^{-5}$ W) throughout the relaxation delay (10 s) and mixing time (30 ms). Gradient pulses for coherence selection were applied using a Z-only gradient (SMSQ10.100) at 92% GPZ, followed by a 200 μ s recovery delay (d16) to diphase unwanted coherences. The degree of acetylation (DA) was quantified via ^1H NMR using Equation (1):

$$DA(\%) = \left[\frac{\frac{1}{3} \times I_{\text{CH}_3}}{I_{\text{H}-2} + (\frac{1}{3} \times I_{\text{CH}_3})} \right] \times 100 \quad (1)$$

$$DD(\%) = 100\% - DA \quad (2)$$

Where I_{CH_3} denotes the integral of the methyl signal of the *N*-acetyl-*D*-glucosamine unit located at δ_{H} 1.93 ppm (Fig. 1B), and $I_{\text{H}-2}$ represents the H-2 proton signal of the non-acetylated glucosamine unit located at δ_{H} 2.6 ppm.

UV-vis spectroscopy: UV-vis analysis was conducted by using a V-780 UV-vis spectrometer (Jasco Corporation, Tokyo, Japan). 10 mg of different NFs were immersed in 5 mL of deionized water for 12 hours, and then 4 mL of the solution was placed in a 5 mm cuvette for testing. The UV-Vis spectral analysis was performed in the wavelength range of 200–400 nm. For release studies, 50 mg of the NF membrane was immersed in 10 mL of deionized water at room temperature. At predetermined time points (10, 20, 40, 60, 80, 100, 120, 180, and 240 minutes), aliquots (0.1 mL) were rapidly tested in 2 mm quartz cuvettes. After the test, the solvent was returned to the original release solution. The results were analyzed at 210 nm.

Water solubility analysis: The water solubility of CS300, CS7, and CS1 were evaluated through visual inspection and turbidimetric analysis, as outlined in a previously documented procedure. Each sample (50 mg) was dissolved in 5 mL of aqueous acetic acid (1%, v/v), and the pH was adjusted to between 4–12 by gradually adding 0.1 M NaOH. The transmittance of the solutions was measured at 600 nm using a V-780 UV-vis photometer (optical range 1 cm, Jasco Corporation, Tokyo, Japan).

Fourier transform infrared spectroscopy (FTIR): The infrared analysis was conducted with a 470 Fourier Transform Infrared Spectrometer (FT-IR, Jasco Corporation, Tokyo, Japan) in attenuated total reflection attachment (ATR) mode, utilizing air as a reference, within the 400–4000 cm^{-1} wavelength range. Each spectrum, composed of 24 scans, was used to identify the functional groups within the CS300, CS7, and CS1 samples. The FT-IR analysis of NFs was conducted using the same procedure.

Acid dissociation constant (pKa) determination of CS300, CS7 and CS1: The pKa of the polymers was determined by ζ -potential measurements of different 1mg/mL polymer aqueous solutions in a range from pH 2 to 12 using a Zetasizer ZS (Malvern Panalytical, UK) equipped with a H-Ne 633 nm laser at 25 °C and with a backscattering of 173°. Obtained data was fitted following a Boltzmann function

with a Pearson correlation coefficient (R^2) > 0.95 and the pKa value was estimated as the absolute minimum of the derivative fitting.

Electrical conductivity of electrospinning solutions: The electrical conductivity of the electrospinning solutions was measured using a digital conductivity meter (Conductimeter Basic 30, CRISON Instruments, Spain) at room temperature (25 °C). Prior to measurement, the instrument was calibrated with standard conductivity solutions of 147 $\mu\text{S}/\text{cm}$ and 12.88 mS/cm at 25 °C. Each solution was measured in triplicate, and the reported values represent the average conductivity, which was used to evaluate the effect of COS type and concentration on the properties of the electrospinning solutions.

Viscosity of electrospinning solutions: The viscosity of the electrospinning solutions was measured using a Cannon–Fenske routine viscometer (size 450, PROTON, Spain) at 40 °C. The viscometer constant was 2.5 mm^2/s^2 . Prior to measurement, each solution was equilibrated at 40 °C to ensure temperature stability. The flow time of each solution was recorded, and the kinematic viscosity was calculated using the following equation (3):

$$\nu = C \times t \quad (3)$$

where ν is the kinematic viscosity (mm^2/s), C is the viscometer constant (mm^2/s^2), and t is the mean flow time (s).

The density of each solution was measured using a density meter (DMA 501, Anton Paar, Austria) at 40 °C, and the dynamic viscosity was calculated using the equation (4):

$$\eta = C \times \rho \quad (4)$$

where η is the dynamic viscosity (mPa·s), C is the kinematic viscosity (mm^2/s), and ρ is the density (g/cm^3). Each solution was measured in triplicate, and the reported values represent the average viscosity, which was used to evaluate the effect of COS type and concentration on the viscosity properties of the electrospinning solutions.

4.6 Characterization of PVA@CS NFs

Morphological characterization of PVA@CS NFs: The morphology of the electrospun NFs was examined using a JSM-6335F (scanning electron microscope (SEM), JEOL Ltd., Tokyo, Japan) working at 15 kV. Discs (ca. 1 cm diameter) were cut and sputter-coated with gold using a Quorum Q150RS coater (Quorum Technologies Ltd., UK) prior to imaging. Fiber diameter and size distribution were determined by analyzing more than 200 fibers per sample using ImageJ software (version 1.53e) from three SEM images ($\times 25,000$ magnification).

Elemental analysis of PVA@CS NFs: Quantification of incorporated CS within the PVA@CS NFs was estimated based on the nitrogen content by a Rapid N elemental analyzer (Elementar Analysensysteme GmbH, Langenselbold, Germany). Approximately 40 mg of each sample was sealed in tin capsules and combusted at 960 °C. The evolved nitrogen-containing gases were separated and quantified using a thermal conductivity detector (TCD), and the results are expressed as nitrogen percentage relative to total fiber mass.

Quantification of released components (PVA, CS) from PVA@CS NFs: The release of PVA, CS1 and CS7 from PVA@CS NFs was



analyzed by ^1H NMR spectroscopy (see SI for details). Initially, 50 mg of electrospun NFs were immersed in 5 ml of water and agitated at room temperature for 24 h. The solution was centrifuged at 6500 rpm for 15 min to eliminate undissolved material, and the supernatant was freeze-dried at $-80\text{ }^\circ\text{C}$ for 24 h. Calibration curves for **CS7**, **CS1**, and PVA were then established (see **Section S1.4** and **Fig. S9**). Next, 5 mL of D_2O was added to the freeze-dried extracts. Samples were heated at $80\text{ }^\circ\text{C}$ for 30 min to ensure total dissolution of PVA. Subsequently, 500 μL of the resulting supernatant were transferred to 5 mm NMR tubes. Spectra were recorded at $300 \pm 0.1\text{ K}$ using a Bruker Avance III 600 MHz NMR spectrometer (Bruker BioSpin GmbH, Germany). with a quadruple resonance cryoprobe Proton spectra were analyzed using TOPSPIN software (version 4.3) and quantified using the ERETIC signal as a reference, calibrated to a 2.3 mM signal of 2,2,3,3-d₄-(trimethylsilyl)propionic acid (TSP).

4.7 Antimicrobial and Wound healing test

Minimal Inhibitory Concentration (MIC) determination: MIC values for *Staphylococcus (S.) aureus* (ATCC 12600), *Escherichia (E.) coli* (K12), *Pseudomonas (P.) aeruginosa* (PA01), and *Candida (C.) albicans* (ATCC 10231) were determined via the standard broth-dilution method in 96-well microlitre plates in Lysogeny Broth (LB) media for bacterial cells and Sabouraud dextrose media for fungal cells. The MIC of each compound was evaluated using a 2-fold decreasing concentration of each sample between 60 - 0.5 mg/mL against a bacterial/fungal inoculum of 10^7 - 10^9 colony-forming units per mL (CFU/mL). Plates were incubated at $37\text{ }^\circ\text{C}$ for 18 h. MIC values were determined as the lowest concentration where no turbidity was observed. Simultaneously, the optical density at 600 nm (OD600) was measured with a SpectraMax iD3 from Molecular Devices (San José, CA, USA) plate reader. MIC values are based on three biological replicates.

Antimicrobial agars contact assays: To assess the antimicrobial activity of the PVA@CS NF composites, ca. 2 cm diameter samples were placed on LB (for bacterial cells) or Sabouraud (for fungal cells) agar plates inoculated with 50 μL of 10^7 - 10^9 CFU/mL. The plates were incubated at $37\text{ }^\circ\text{C}$ for 18 h in the case of the bacteria cells and 48 h for fungal samples. Then, the CFU under the NF patch was enumerated. Depicted results (average \pm SD) are based on 3 biological replicates.

Wound-healing experiments: HaCaT (human keratinocyte cell line) cells were cultured in Dulbecco's Modified Eagle Medium (DMEM) medium supplemented with 10 % (v/v) heat inactivated fetal bovine serum (FBS) in a highly humidified atmosphere of 95 % air with 5 % CO_2 at $37\text{ }^\circ\text{C}$. Cell splitting was performed every 72 h (70-80 % confluent), adding Trypsin-EDTA solution (0.25 %) for 15 min at $37\text{ }^\circ\text{C}$ and blocking by means of DMEM-10 % FBS complete cell culture medium. For the *in vitro* wound scratch Assays, HaCaT cells were seeded in a 24-well plate at a cell density of 250000 cells/well reaching a completely confluent cell monolayer. The cell monolayer was scratched in a straight line with a p100 micropipette tip. PVA (1, 0.1 and 0.01 mg/mL) and chitosan solutions (0.1 and 0.01 mg/mL concentrations) were added on top of the "wounded" cells and the gap closure was followed at time points 0, 3, 6, 24 and 48 h using bright-field microscopy (Nikon Eclipse Ts2R, Nikon Corp., Tokyo, Japan).

Author contributions

L.L and A.R.M contributed to experimental data, formal analysis, investigation, and writing of the original draft. F.A.C. and S.F.G. were responsible for MwOSY and NMR release experiments, respectively. N.M.F. contribute to the release experiments. T.F. and J.L. contribute to wound healing assays and microbiological assessment. I.F. contributes with funding acquisition, supervision, data analysis, and manuscript writing and revision. R.C.C. and P.G. provided conceptualization, supervision, funding acquisition, writing, review, and editing.

Conflicts of interest

The authors declare no competing financial interest.

Data availability

The data supporting this article are provided in the supplementary information (SI). See DOI:

Acknowledgements

This work was supported by the State Research Agency of the Spanish Ministry of Science and Innovation under Grant Nos. CNS2022-135583, PID2021-122645OB-I00, CPP2022-009967 and PID2021-127983OB-C22, by the Spanish Government (MCIN/AEI/10.13039/501100011033) and the European Union "Next Generation EU"/PRTR. The authors also acknowledge financial support from the Generalitat de Catalunya through AGAUR Grants No. 2021SGR00446 and 2021SGR00135, and from the "Severo Ochoa" Programme for Centers of Excellence in R&D funded by MCIN and FEDER ("A way of making Europe") under Grant No. CEX2023-001263-S. Individual funding is acknowledged from the MCIN/AEI "Ramón y Cajal" Programme and the European Social Fund "FSE invierte en tu futuro" under Grant Nos. RYC2019-028414 and RYC2021-03447-I. Additional postdoctoral support was provided through the María Zambrano and Beatriu de Pinós fellowship programmes. Financial support from the Plan Propio de Investigación y Transferencia 2023 of the University of Almería is also acknowledged (ref. ARyC2023_01). L.L. acknowledges the Chinese Scholarship Council for her predoctoral fellowship (Grant No. 202206650005).

References

- 1 G. Maheshwari, *Wounds APAC*.
- 2 M. Olsson, K. Järbrink, U. Divakar, R. Bajpai, Z. Upton, A. Schmidtchen and J. Car, *Wound repair and regeneration*, 2019, **27**, 114–125.
- 3 A. Patel, P. Halder, J. Manahy, R. Pal, S. Ashique, S. Ghosh, S. Ghazanfar and F. Taghizadeh-Hesary, in *Nanomaterials for Wound Healing*, CRC Press, 2025, pp. 45–70.
- 4 M. Farahani and A. Shafiee, *Adv. Healthc. Mater.*, 2021, **10**, 2100477.



- 5 Y. Zhong, E. Wei, L. Wu, Y. Wang, Q. Lin, N. Wu, H. Chen and N. Tang, *ACS Omega*, 2024, **9**, 32268–32286.
- 6 Y. Jiang, A. A. Trotsyuk, S. Niu, D. Henn, K. Chen, C.-C. Shih, M. R. Larson, A. M. Mermin-Bunnell, S. Mittal and J.-C. Lai, *Nat. Biotechnol.*, 2023, **41**, 652–662.
- 7 R. Lemos, F. R. Maia, R. L. Reis and J. M. Oliveira, *Adv. Nanobiomed Res.*, 2022, **2**, 2100116.
- 8 Z. G. Chen, P. W. Wang, B. Wei, X. M. Mo and F. Z. Cui, *Acta Biomater.*, 2010, **6**, 372–382.
- 9 J. Liu, Q. Song, W. Yin, C. Li, N. An, Y. Le, Q. Wang, Y. Feng, Y. Hu and Y. Wang, in *Exploration*, Wiley Online Library, 2025, vol. 5, p. 20230078.
- 10 M. Abrigo, S. L. McArthur and P. Kingshott, *Macromol. Biosci.*, 2014, **14**, 772–792.
- 11 A. K. Gaharwar, I. Singh and A. Khademhosseini, *Nat. Rev. Mater.*, 2020, **5**, 686–705.
- 12 S. Nam and D. Mooney, *Chem. Rev.*, 2021, **121**, 11336–11384.
- 13 Y. Yang, Y. Du, J. Zhang, H. Zhang and B. Guo, *Advanced Fiber Materials*, 2022, **4**, 1027–1057.
- 14 A. Libanori, G. Chen, X. Zhao, Y. Zhou and J. Chen, *Nat. Electron.*, 2022, **5**, 142–156.
- 15 G. Chen, X. Xiao, X. Zhao, T. Tat, M. Bick and J. Chen, *Chem. Rev.*, 2021, **122**, 3259–3291.
- 16 T. C. Mokhena, M. B. Chabalala, S. Mapukata, A. Mtibe, L. Hlekelele, Z. Cele, M. J. Mochane, B. Ntsendwana, T. A. Nhlapo and T. P. Mokoena, *Macromol. Mater. Eng.*, 2024, **309**, 2300388.
- 17 M. Tavakoli, S. Labbaf, M. Mirhaj, S. Salehi, A. M. Seifalian and M. Firuzeh, *J. Appl. Polym. Sci.*, 2023, **140**, e53910.
- 18 B. Azimi, M. Milazzo, A. Lazzeri, S. Berrettini, M. J. Uddin, Z. Qin, M. J. Buehler and S. Danti, *Adv. Healthc. Mater.*, 2020, **9**, 1901287.
- 19 B. Sheokand, M. Vats, A. Kumar, C. M. Srivastava, I. Bahadur and S. R. Pathak, *Journal of polymer science*, 2023, **61**, 1389–1414.
- 20 P. Sahariah and M. Másson, *Biomacromolecules*, 2017, **18**, 3846–3868.
- 21 M. N. V. R. Kumar, R. Muzzarelli, C. Muzzarelli, H. Sashiwa and A. J. Domb, *Chem. Rev.*, 2004, **104**, 6017–6084.
- 22 D. Duymaz, A. O. Kebabcı and S. Kizilel, *Int. J. Biol. Macromol.*, 2025, 142055.
- 23 M. Arshad, M. Zubair and A. Ullah, in *Handbook of chitin and chitosan*, Elsevier, 2020, pp. 377–399.
- 24 M. Kucharska, M. Sikora, K. Brzoza-Malczewska and M. Owczarek, *Chitin and Chitosan: Properties and Applications*, 2019, 169–187.
- 25 M. Másson, *Carbohydr. Polym.*, 2024, **337**, 122159.
- 26 T. Jiang, M. Deng, R. James, L. S. Nair and C. T. Laurencin, *Acta Biomater.*, 2014, **10**, 1632–1645.
- 27 D. Alemu, E. Getachew and A. K. Mondal, *Int. J. Polym. Sci.*, 2023, **2023**, 5025341.
- 28 Y. Li, Y. Yang, Z. Huang, Z. Luo, C. Qian, Y. Li and Y. Duan, *Int. J. Biol. Macromol.*, 2021, **187**, 441–450.
- 29 J. C. Fernandes, F. K. Tavarıa, J. C. Soares, Ó. S. Ramos, M. J. Monteiro, M. E. Pintado and F. X. Malcata, *Food Microbiol.*, 2008, **25**, 922–928.
- 30 W. Janvikul, P. Ngamviriyavong, P. Uppanun, P. Tanjak and N. Sangjun, in *Advanced Materials Research*, 2012, vol. 306, pp. 31–34.
- 31 H. Jafari, K. V. Bernaerts, G. Dodi and A. Shavandi, *Materials Science and Engineering: C*, 2020, **117**, 111266.
- 32 Y.-T. Jia, J. Gong, X.-H. Gu, H.-Y. Kim, J. Dong and X.-Y. Shen, *Carbohydr. Polym.*, 2007, **67**, 403–409.
- 33 R. R. Klossner, H. A. Queen, A. J. Coughlin and W. E. Krause, *Biomacromolecules*, 2008, **9**, 2947–2953.
- 34 C. Zhou and Q. Wu, *Colloids Surf. B Biointerfaces*, 2011, **84**, 155–162.
- 35 A. Turanlı, C. Altinkok, E. C. Kacakgil, C. Dizman and G. Acik, *Int. J. Biol. Macromol.*, 2025, **315**, 144467.
- 36 K. G. Nathan, K. Genasan and T. Kamarul, *Mar. Drugs*, 2023, **21**, 304.
- 37 M. A. Ibrahim, M. H. Alhalafi, E.-A. M. Emam, H. Ibrahim and R. M. Mosaad, *Polymers (Basel)*, 2023, **15**, 2820.
- 38 Z. Shariatinia, *Int. J. Biol. Macromol.*, 2018, **120**, 1406–1419.
- 39 K. Pathak, S. K. Misra, A. Sehgal, S. Singh, S. Bungau, A. Najda, R. Gruszecki and T. Behl, *Polymers (Basel)*, 2021, **13**, 2514.
- 40 A. Akbari, S. Rabbani, S. Irani, M. Zandi, F. Sharifi, F. Ameli and M. Mohamadali, *J. Appl. Polym. Sci.*, 2022, **139**, 51764.
- 41 Z. Fang, W. Cong, H. Zhou, J. Zhang and M. Wang, *J. Funct. Foods*, 2024, **116**, 106219.
- 42 S. Nain, R. Singh and S. Ravichandran, *Advanced Journal of Chemistry-Section A*, 2019, **2**, 94–104.
- 43 H. Tan, R. Ma, C. Lin, Z. Liu and T. Tang, *Int. J. Mol. Sci.*, 2013, **14**, 1854–1869.
- 44 N. Haneishi, S. Tsubaki, E. Abe, M. M. Maitani, E. Suzuki, S. Fujii, J. Fukushima, H. Takizawa and Y. Wada, *Sci. Rep.*, 2019, **9**, 222.
- 45 K. Li, R. Xing, S. Liu, Y. Qin, X. Meng and P. Li, *Int. J. Biol. Macromol.*, 2012, **51**, 767–773.
- 46 K. L. B. Chang, M.-C. Tai and F.-H. Cheng, *J. Agric. Food Chem.*, 2001, **49**, 4845–4851.
- 47 M. Tian, H. Tan, H. Li and C. You, *RSC Adv.*, 2015, **5**, 69445–69452.
- 48 F. M. Arrabal-Campos, L. M. Aguilera-Sáez and I. Fernández, *J. Phys. Chem. A*, 2019, **123**, 943–950.
- 49 K. Xu and S. Zhang, *Anal. Chem.*, 2014, **86**, 592–599.
- 50 F. M. Arrabal-Campos, P. Oña-Burgos and I. Fernández, *Polym. Chem.*, 2016, **7**, 4326–4329.
- 51 F. M. Arrabal-Campos, M. Gonzalez-Lazaro, J. M. Pérez, J. A. M. Lao and I. Fernandez, *Eur. Polym. J.*, 2025, **226**, 113710.
- 52 D. Kurpan, M. Ciardi, L. Pessôa, S. Belachqer-El Attar, A. Schievano, A. C. Abreu, I. Fernández, A. Ida and G. Acién, *J. Environ. Chem. Eng.*, 2025, 119570.
- 53 N. N. Duy, D. Van Phu, N. T. Anh and N. Q. Hien, *Radiation Physics and Chemistry*, 2011, **80**, 848–853.
- 54 T. Sun, D. Zhou, J. Xie and F. Mao, *European Food Research and Technology*, 2007, **225**, 451–456.
- 55 C. Q. Qin, Y. M. Du and L. Xiao, *Polym. Degrad. Stab.*, 2002, **76**, 211–218.



- 56 R. A. A. Muzzarelli, F. Tanfani, M. Emanuelli and S. Mariotti, *Carbohydr. Res.*, 1982, **107**, 199–214.
- 57 M. Tian, F. Chen, D. Ren, X. Yu, X. Zhang, R. Zhong and C. Wan, *Carbohydr. Polym.*, 2010, **79**, 137–144.
- 58 X. Guo, T. Sun, R. Zhong, L. Ma, C. You, M. Tian, H. Li and C. Wang, *Front. Pharmacol.*, 2018, **9**, 1412.
- 59 M. S. Khoshkhoo, F. A. Taromi, E. Kowsari and E. K. Shalamzari, *Polymer (Guildf.)*, 2013, **54**, 4017–4029.
- 60 S. K. Kim, *Chitooligosaccharides: Prevention and control of diseases*, Springer International Publishing, 2022.
- 61 M. Rajabi, J. Cabral, S. Saunderson and M. A. Ali, *Carbohydr. Polym.*, 2022, **295**, 119884.
- 62 N. Bhattarai, D. Edmondson, O. Veiseh, F. A. Matsen and M. Zhang, *Biomaterials*, 2005, **26**, 6176–6184.
- 63 D. R. Salem, in *Nanofibers and nanotechnology in textiles*, Elsevier, 2007, pp. 3–21.
- 64 C. Zhang, X. Yuan, L. Wu, Y. Han and J. Sheng, *Eur. Polym. J.*, 2005, **41**, 423–432.
- 65 J. M. Deitzel, J. Kleinmeyer, D. E. A. Harris and N. C. B. Tan, *Polymer (Guildf.)*, 2001, **42**, 261–272.
- 66 Z. M. Huang, Y. Z. Zhang, M. Kotaki and S. Ramakrishna, *Compos. Sci. Technol.*, 2003, **63**, 2223–2253.
- 67 D. H. Reneker and I. Chun, *Nanotechnology*, 1996, **7**, 216.
- 68 A. Smeets, C. Clasen and G. Van den Mooter, *European Journal of Pharmaceutics and Biopharmaceutics*, 2017, **119**, 114–124.
- 69 S. Promnil, P. O. Numpaisal and Y. Ruksakulpiwat, *Mater. Today Proc.*, 2021, **47**, 3496–3499.
- 70 A. C. Mendes, J. Sevilla Moreno, M. Hanif, T. EL Douglas, M. Chen and I. S. Chronakis, *Int. J. Mol. Sci.*, 2018, **19**, 2266.
- 71 S. Kubo and J. F. Kadla, *Biomacromolecules*, 2003, **4**, 561–567.
- 72 G. C. da Mata, M. S. Morais, W. P. de Oliveira and M. L. Aguiar, *Polymers (Basel)*, 2022, **14**, 4856.
- 73 L. G. Gómez-Mascaraque, G. Sanchez and A. López-Rubio, *Carbohydr. Polym.*, 2016, **150**, 121–130.
- 74 E. M. Darby, E. Trampari, P. Siasat, M. S. Gaya, I. Alav, M. A. Webber and J. M. A. Blair, *Nat. Rev. Microbiol.*, 2023, **21**, 280–295.
- 75 I. Wiegand, K. Hilpert and R. E. W. Hancock, *Nat. Protoc.*, 2008, **3**, 163–175.
- 76 B. Gottenbos, D. W. Grijpma, H. C. van der Mei, J. Feijen and H. J. Busscher, *Journal of antimicrobial chemotherapy*, 2001, **48**, 7–13.
- 77 A. Lo Sciuto and F. Imperi, *Antimicrob. Agents Chemother.*, 2018, **62**, 10–1128.
- 78 A. Lo Sciuto, M. Cervoni, R. Stefanelli, C. Mancone and F. Imperi, *Int. J. Antimicrob. Agents*, 2020, **55**, 105957.
- 79 S. Yokota, H. Hakamada, S. Yamamoto, T. Sato, T. Shiraishi, M. Shinagawa and S. Takahashi, *Int. J. Antimicrob. Agents*, 2018, **51**, 888–896.
- 80 M. Kong, X. G. Chen, K. Xing and H. J. Park, *Int. J. Food Microbiol.*, 2010, **144**, 51–63.
- 81 E. I. Rabea, M. E.-T. Badawy, C. V. Stevens, G. Smagghe and W. Steurbaut, *Biomacromolecules*, 2003, **4**, 1457–1465.
- 82 B. K. Tiwari, V. P. Valdramidis, C. P. O'Donnell, K. Muthukumarappan, P. Bourke and P. J. Cullen, *J. Agric. Food Chem.*, 2009, **57**, 5987–6000.
- 83 R. C. Goy, D. de Britto and O. B. G. Assis, *Polímeros*, 2009, **19**, 241–247.
- 84 J. C. V. Ribeiro, T. C. M. Forte, S. J. S. Tavares, F. K. Andrade, R. S. Vieira and V. Lima, *J. Biomed. Mater. Res. A*, 2021, **109**, 2556–2569.
- 85 W. Niu, Y. Dong, Z. Fu, J. Lv, L. Wang, Z. Zhang, J. Huo and J. Ju, *Int. J. Biol. Macromol.*, 2021, **193**, 1927–1936.
- 86 C. Gonçalves, N. Ferreira and L. Lourenço, *Polymers 2021, Vol. 13, Page 2466*, 2021, **13**, 2466.
- 87 H. D. Jhundo, T. Siefen, A. Liang, C. Schmidt, J. Lokhnauth, A. Béduneau, Y. Pellequer, C. C. Larsen and A. Lamprecht, *Pharmaceutics 2020, Vol. 12, Page 1038*, 2020, **12**, 1038.
- 88 C. Muanprasat, P. Wongkrasant, S. Satitsri, A. Moonwiriya, P. Pongkorpsakol, T. Mattaveewong, R. Pichyangkura and V. Chatsudthipong, *Biochem. Pharmacol.*, 2015, **96**, 225–236.
- 89 T. Mehmood, R. Pichyangkura and C. Muanprasat, *Polymers 2023, Vol. 15, Page 1681*, 2023, **15**, 1681.
- 90 V. S. Yadav, K. Makker, R. Haidrus, A. Dawar and B. Gumber, *J. Periodontal Res.*, 2024, **59**, 1153–1161.
- 91 T. Minagawa, Y. Okamura, Y. Shigemasa, S. Minami and Y. Okamoto, *Carbohydr. Polym.*, 2007, **67**, 640–644.
- 92 T. Mori, M. Okumura, M. Matsuura, K. Ueno, S. Tokura, Y. Okamoto, S. Minami and T. Fujinaga, *Biomaterials*, 1997, **18**, 947–951.
- 93 R. Jayakumar, D. Menon, K. Manzoor, S. V. Nair and H. Tamura, *Carbohydr. Polym.*, 2010, **82**, 227–232.
- 94 R. A. A. Muzzarelli, *Carbohydr. Polym.*, 2009, **76**, 167–182.
- 95 J. S. Boateng, K. H. Matthews, H. N. E. Stevens and G. M. Eccleston, *J. Pharm. Sci.*, 2008, **97**, 2892–2923.
- 96 K. Wei, Y. Li, K. Kim, Y. Nakagawa, B. Kim, K. Abe, G. Chen and I. Kim, *J. Biomed. Mater. Res. A*, 2011, **97**, 272–280.
- 97 A. Biswal, S. S. Purohit and S. K. Swain, *J. Drug Deliv. Sci. Technol.*, 2023, **84**, 104549.
- 98 H. Liu, R. Chen, P. Wang, J. Fu, Z. Tang, J. Xie, Y. Ning, J. Gao, Q. Zhong, X. Pan, D. Wang, M. Lei, X. Li, Y. Zhang, J. Wang and H. Cheng, *Carbohydr. Polym.*, 2023, **316**, 121050.
- 99 N. R., K. M., P. J., V. K.S., C. Arpana, P. Balashanmugam and G. D. Venkatasubbu, *Colloids Surf. B Biointerfaces*, 2019, **182**, 110339.
- 100 H. Guo, H. Luo, J. Ou, J. Zheng, C. Huang, F. Liu and S. Ou, *Carbohydr. Polym.*, 2025, **348**, 122822.
- 101 N. D. Tien, T. Geng, C. A. Heyward, J. E. Reseland, S. P. Lyngstadaas, J. J. Blaker and H. J. Haugen, *Biomaterials Advances*, 2022, **137**, 212871.
- 102 M. Mahdian-Dehkordi, F. Sarrafzadeh-Rezaei, M. Razi and M. Mahmoudian, *Veterinary Research Forum*, 2021, **12**, 25–32.
- 103 X. Zhang, Y. Liang, S. Huang and B. Guo, *Adv. Colloid Interface Sci.*, 2024, **332**, 103267.
- 104 H. Liu, C. Wang, C. Li, Y. Qin, Z. Wang, F. Yang, Z. Li and J. Wang, *RSC Adv.*, 2018, **8**, 7533–7549.



- 105 X. Wang, R. Song, M. Johnson, A. Sigen, P. Shen, N. Zhang, I. Lara-Sáez, Q. Xu and W. Wang, *Macromol. Biosci.*, 2023, **23**, 2300094.
- 106 H. Jafari, C. Delporte, K. V. Bernaerts, G. De Leener, M.

View Article Online
DOI: 10.1039/D6TB00497K

Formatting – please delete this box prior to submission

- Our template aims to give you an idea of what your article will look like, however the final version will be formatted in our house style and may look different.
- Please consult the Styles menu for recommended formatting for all text, including footnotes, references, tables, images and captions.
- Text should not be wrapped around graphics.

During production:

- Graphics, including tables, will be located at the top or bottom of the column following their first citation in the text. Graphics can be single column or double column as appropriate and require captions.
- Equations will be placed in the flow of the text.
- Sufficient space will be inserted around graphics for clarity of reading; a horizontal bar will also be used to separate all inserted graphics, tables and their captions from the text.

If you are experiencing difficulty using our template, please consult our 'Using the Template' guide, found [here](#).

Luhmer, L. Nie and A. Shavandi, *Chemical Engineering Journal Advances*, 2021, **7**, 100113.

Notes and references



DATA AVAILABILITY STATEMENT

View Article Online
DOI: 10.1039/D6TB00497K

The supporting data has been provided as part of the Supplementary information.

Table of Content

Supporting Experimental Content

1.1 Determination of the elemental nitrogen content in **CS7** and **CS1** and the encapsulation efficiency in PVA@CS NFs.

1.2 Calculation of theoretical mass and theoretical percentage of N, experimental mass, experimental percentage of nitrogen, experimental percentage of CSs and EE for PVA@NFs.

1.3 Molecular weight determination via diffusion NMR.

1.4 Release experiments.

Supporting Tables

Table S1. Summary of the feeding amounts of **CS1**, **CS7**, and PVA used in the production of PVA@CS NFs. Theoretical weight percentages of CS and PVA in the NFs. Nitrogen weight percentages calculated from theoretical and elemental analyses. Mass of CS in PVA@CS NFs calculated from the nitrogen content.

Table S2. Summary of the weight percent release of **CS1**, **CS7**, and PVA from PVA@**CS1** and PVA@**CS7** after 24 hours, quantified by ¹H NMR spectroscopy. CS and PVA release efficiency and CS mass released per mg of NFs.

Table S3. Minimal Inhibitory Concentration (MIC) values (mg/mL) of PVA, **CS300**, **CS7** and **CS1** for *C. albicans* (ATCC 10231) determined by the 2-fold dilution method at 37 °C under mild shaking in LB media. Depicted results are based on three biological replicates.

Table S4. Amount of PVA, CS and milliliters of DMF, AcOH (20%, v/v) and H₂O used for fabrication of the PVA NFs, PVA@CS1-1~5 NFs and PVA@CS7-1~5 NFs.



Supporting Figures

Fig. S1 Characterization of **CS300** (red line), **CS7** (blue line) and **CS1** (green line). A) UV-vis spectra of **CS300**, **CS7** and **CS1** at pH 5.5 (1 mg/mL). B) Water solubility of **CS300**, **CS7** and **CS1** with pH in the pH range 4-12 at 0.2 w/v%.

Fig. S2. pKa estimation of CS samples. A) Derivative of the ζ -potential distribution at different pH values and B) the relationship between the calculated Molecular Weight (MW) and the pKa.

Fig. S3 Morphology and diameter statistics of pure PVA NFs. A) Representative SEM image of PVA NFs. B) Diameter analysis of PVA NFs.

Fig. S4 Dimensional analysis of PVA@CS1 NFs and PVA@CS7 NFs (200 nanofibers). A) PVA@CS1-1, B) PVA@CS7-1, C) PVA@CS1-2, D) PVA@CS7-2, E) PVA@CS1-3, F) PVA@CS7-3, G) PVA@CS1-4, H) PVA@CS7-4, I) PVA@CS1-5, and J) PVA@CS7-5.

Fig. S5 Electrical conductivity characterization of PVA@CS1 (green line) and PVA@CS7 (blue) series electrospun solutions. A) CS1 content versus electrical conductivity in PVA@CS1 nanofibers. B) **CS7** content versus electrical conductivity in PVA@CS7 nanofibers. C) Electrical conductivity versus CS content for PVA@CS1 and PVA@CS7 series.

Fig. S6. A) Comparison of FTIR spectra of PVA NFs, PVA@CS1-1~5 and **CS1**. B) Comparison of UV-vis spectra of PVA NFs, PVA@CS1-1~5 and **CS1**. C) Comparison of FTIR spectra of PVA NFs, PVA@CS7-1~5 and **CS7**. D) Comparison of UV-vis spectra of PVA NFs, PVA@CS7-1~5 and **CS7**.

Fig. S7. Schematic representation of possible accumulation of CS molecules at the surface of the PVA NFs produced at higher percentages of **CS1** and **CS7**.

Fig. S8. Calibration lines obtained from NMR studies for A) PVA, B) **CS7** and C) **CS1**.

Fig. S9. UV-vis spectra of CS release from PVA@CS NFs in water at different time points. (A)PVA@CS1-2; (B) PVA@CS1-5;(C) PVA@CS7-2;(D) PVA@CS7-5.

Fig. S10. Measurements of cell density (optical density at 600 nm, OD600) of A) *S. aureus* (ATCC 12600), B) *E. coli* (K12) and C) *P. aeruginosa* (PA01) in LB as a function of PVA, **CS300**, **CS7** and **CS1** concentration. The cultures were incubated at 37 °C for 18 h before the measurements. Depicted values (average \pm SD) are based on 3 biological replicas.



Fig. S11. Measurements of cell density (optical density at 600 nm, OD600) of *C. albicans* (ATCC 10231) in A) Sabouraud (pH 5.5) and B) LB (pH 7.4) media as a function of PVA, **CS300**, **CS7** and **CS1** concentration. The cultures were incubated at 37 °C for 18 h before the measurements. Depicted values (average ± SD) are based on 3 biological replicas.

Fig. S12. Representative images of PVA@CS7 NF disks incubated overnight in agar previously inoculated with *E. coli* (K12).

Fig. S13. Weight distribution of A) PVA@CS1 and B) PVA@CS7 NFs disks for microbial detection and estimated release from C) **CS7** or D) **CS1**.

Fig. S14. Quantification of the wound width over time of HaCaT-ras A5 cell culture in presence of A) PVA, B) **CS1** and C) **CS7** at different concentrations, and D) the estimated wound healing rate. Statistical significance was determined by one-way ANOVA, ns: $p > 0.05$, *: $0.05 > p > 0.01$, **: $0.01 > p > 0.001$, and ***: $p < 0.001$

Fig. S15. Representative images of HaCaT-ras A5 cells proliferation in the presence of PVA, **CS1**, and **CS7** at different concentrations (scale bar = 100 μm).

Fig. S16. Representative images of HaCaT-ras A5 cells proliferation in the absence (untreated) and in the presence of PVA and PVA@CS7 NF (scale bar = 100 μm).

Fig. S17. Schematic representation for the fabrication of the NFs by the electrospinning including photographic images of the electrospinning process after 15 and 60 min.

